Supporting Information

Di- vs tetra-substituted quinonediimines: a drastic effect in coordination chemistry

Lucien Lavaud, Zhongrui Chen, Mourad Elhabiri, Denis Jacquemin*, Gabriel Canard, and Olivier Siri*

S1. Computational details

We have used the Gaussian09 program[1] to perform all our DFT computations, applying default thresholds and algorithms, except when noted below. All calculations relied on the M06 hybrid exchange-correlation functional,[2,3] as this functional provides accurate vertical transition energies,[4] and was successfully applied in similar systems.[5] We have used the 6-31G(d) atomic basis set for all atoms but the Pt centres that were described with the LanL08(*f*) basis set and pseudopotentials. We have performed geometry optimization of the ground-state structures followed by calculations of the vibrational frequencies, confirming the absence of imaginary frequencies. The vertical absorption spectrum were computed with TD-DFT (*Time-Dependent Density Functional Theory*) using the same functional and the diffuse-containing 6-31+G(d) atomic basis set. Environmental effects have been accounted at all steps of the calculations for using the well-known PCM model,[6] applying the linear-response approach in its non-equilibrium limit for the TD-DFT part.[7] The NICS (*Nucleus Independent Chemical Shifts*) reported in the main text have been determined at the M06/cc-pVTZ level. To represent the UV/Vis spectra, we used with the vertical TD-DFT energies and applied a broadening Gaussian of HWHM of 0.25 eV (**2a**) or 0.20 eV (**13**). A contour threshold of 0.02 au is used to represents the molecular orbitals (MOs). The single point CC2 calculations were performed with the Turbomole program[8] using the RI approach and the *def2*-TZVPP basis set.

S2. Theoretical analysis

S2a. Protonation site of 2a

The geometrical structure of **2a** as optimized by DFT in methanol is displayed in **Fig. S1**. Clearly, the theoretical structure is close to the one obtained by XRD (see **Fig. 1**), with the left-hand-side Ph(OMe)$_3$ moiety significantly twisted compared to the plane of the **QDI** whereas the right-hand-side Ph(OMe)$_3$ group is more coplanar. To determine the first protonation site of **2a**, we have determined the Gibbs enthalpies of the possible products, that is protonation of N(2) or N(4) in **Fig. 1** in the body of the publication. The optimal structures are given in **Fig. S1**. We found that the two structures have very close energy, *e.g.,* the differences between the energies of the two species are ca. 1.1 kcal/mol with DFT (in favour of N(4) protonation) but -1.7 kcal/mol with CC2 (in favour of N(2) protonation) in gas-phase. The DFT free energies and solvated energies are also close from one another. Therefore, we have modelled the absorption spectra of the two forms. The results are displayed in **Fig. S2.**
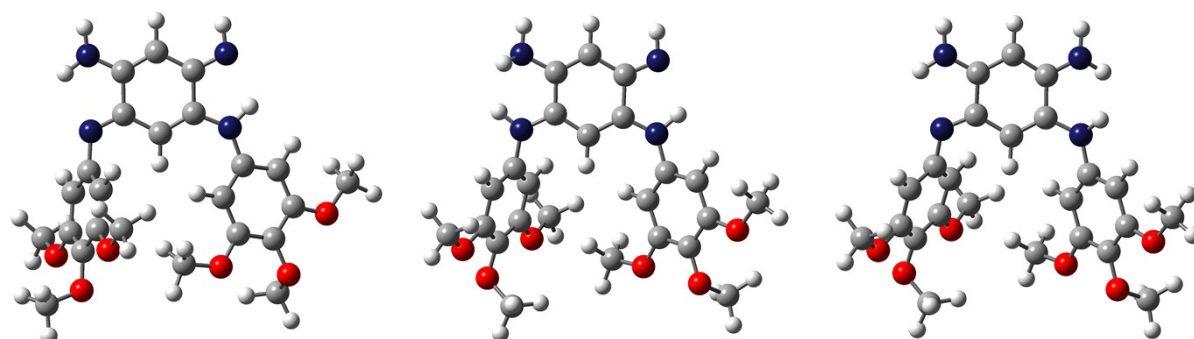
Figure S1. Optimized structures of **2a** (left) and the two possible mono-protonated forms, centre: protonation on N(2), right: protonation on N(4).

As can be seen, the spectra of **2a** nicely fits experiment (**Fig. 3)**. More discussion regarding the nature of the bands in **2a** can be found below.
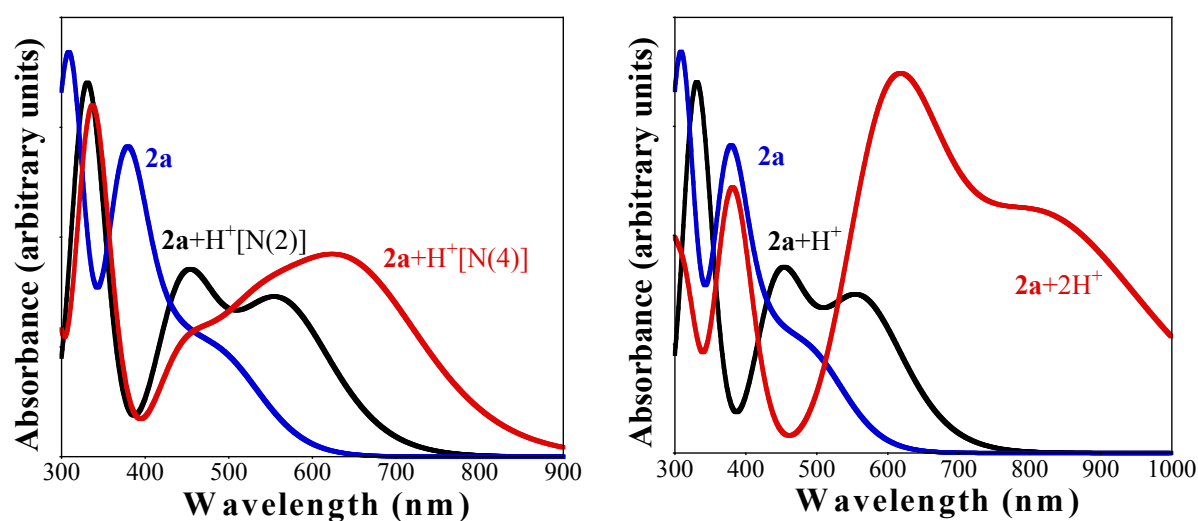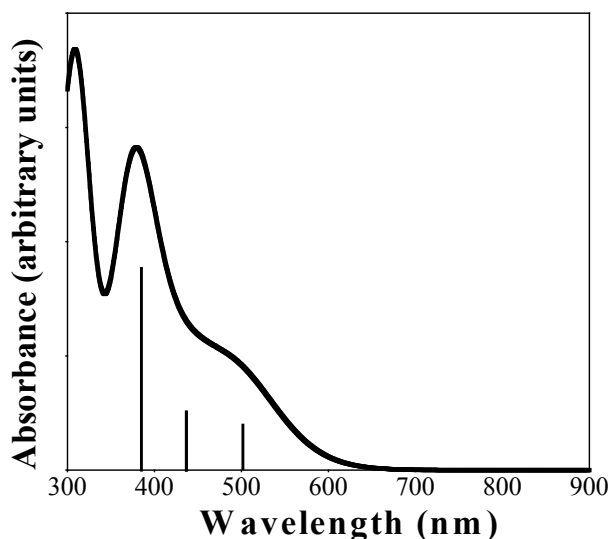

Figure S2. Computed UV/Vis spectrum of **2a** and its two monoprotonated forms (left) and both the monoprotonated and diprotonated forms (right)

In addition, the spectra computed for the protonation on the N(2) site is reasonably matching the experimental curves (see **Fig. 2**), whereas the protonation on the N(4) yields a significantly too red shifted theoretical spectrum with a strong absorption at 700 nm, absent in the experiment. We therefore conclude that the first protonation takes place on N(2), which is consistent with the energies determined with the most accurate method used here, that is, CC2. On the right-hand-side of **Fig. S2,** we compare the neutral, mono-protonated and doubly-protonated **2a** and a noticeable increase in the absorption wavelength is obtained, which also fits experimental trends, though the trends is strongly exaggerated by theory in this case.

S2b. UV/Vis spectra of 2a, 12, 13, 14 and 15

TD-DFT was used to model the optical spectrum of **2a**, **12**, **13**, **14** and **15**. For the former the results are displayed in **Fig. S3**. As stated above, the shape of the curve nicely fits its experimental counterpart (see **Fig. 4**), with a broad absorption in the 400-550 nm region and an intense peak slight below 400 nm. For 2a, TD-DFT reveals that the absorbance in these regions is due to three lowest excited-states, S_1, S_2 and S_3 (see sticks in **Fig. S3**) computed at 501 nm (f=0.068), 436 nm (f=0.077) and 379 nm (f=0.230), respectively. These states can be mainly ascribed to HOMO to LUMO, HOMO-1 to LUMO and HOMO-2 to LUMO electronic promotions, respectively. These orbitals are displayed in **Fig. S4**. As can be seen, the lowest virtual orbital is mainly localised on the **QDI** moiety whereas the occupied orbitals all imply significant contributions from the side trimethoxy-phenyl rings. Therefore, the **QDI** acts here as an acceptor and all states, but especially the two lowest energy ones, present a significant charge-transfer character.


Figure S3. Computed UV/Vis spectrum of **2a**: "*stick*" representation of the three lowest states and convolution resulting from the fifteen lowest excited-states.

HOMO-2   HOMO-1   HOMO   LUMO
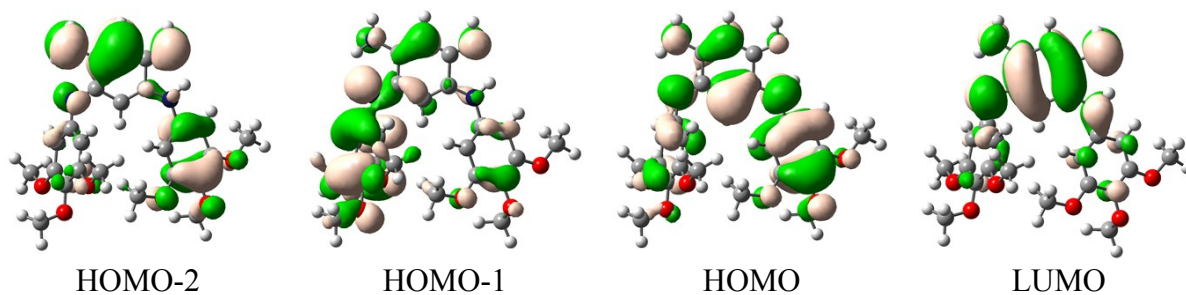
Figure S4. Key MOs of **2a** (contour threshold: 0.02 au)

In **12**, TD-DFT predicts that the first excited-state is located at 652 nm, but it is dipole inactive (f=0.000), so that the second excited-state computed at 483 nm is strongly dipole-allowed (f=0.711) and corresponds to the observed band at 504 nm. This transition is dominated by a HOMO-1 to LUMO character. **Fig. S5** presents these two orbital as well as the electronic density difference (EDD) plots corresponding to this second state. The excited-state is slightly asymmetric and presents a mixed MLCT/IL character (from the Pt to the QDI core with also intra-QDI).
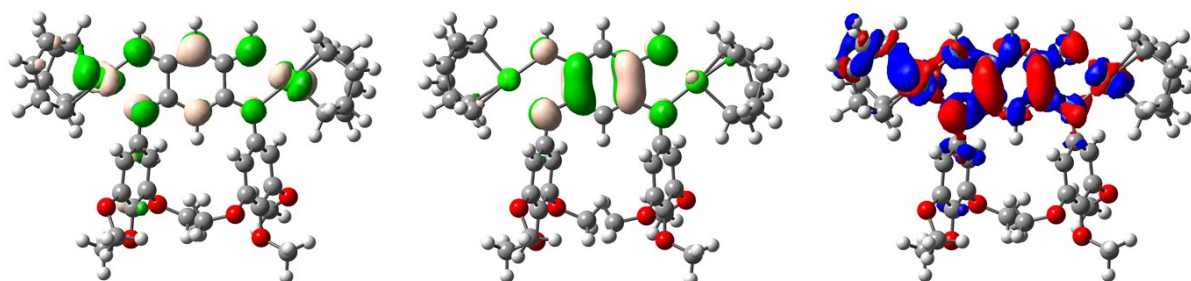
Figure S5. From left to right: HOMO-1, LUMO and density difference plot of the S_2 for **12** (threshold: 0.04 au). In the latter, the blue and red regions indicate zones of decrease and increase of electron density upon transition (contour threshold: 0.001 au).

In **13**, TD-DFT predicts that the two first dipole-allowed states are located at 788 nm (f=0.289, S_1) and 522 nm (f=1.038, S_4), that correspond to the broad band at 800-900 nm and the sharp peak at 565 nm, respectively (see **Fig. S6** and **Fig. 4**). As stated in the main text, these two states can be mainly ascribed to HOMO to LUMO and HOMO-2 to LUMO transitions, respectively. The density difference plot corresponding to the first state is displayed on the r.h.s. of **Fig. S6.**
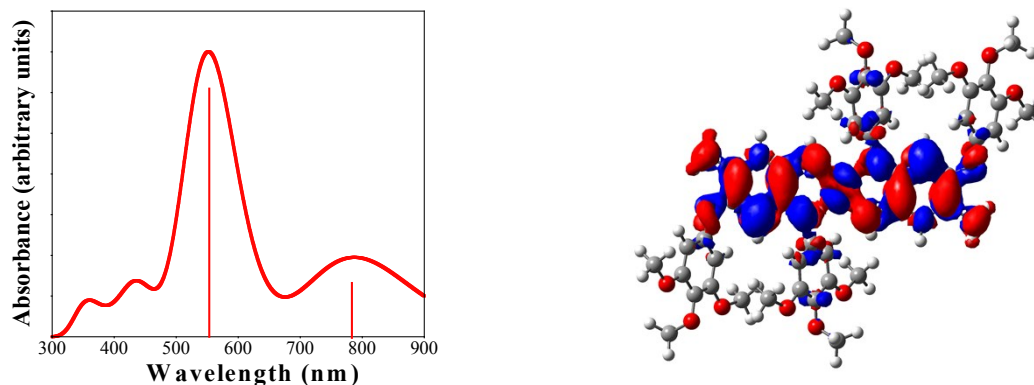

Figure S6. Left: computed UV/Vis spectrum of **13**: "stick" representation of the two lowest states and convolution. Right: EDD plot for the first excited-state of **13** (contour: 0.0004 au).

In **14**, DFT predicts structure belonging to the C_i point group. TD-DFT yields only one strongly dipole-allowed state (S_3 state, A_u symmetry) in the 400-800 nm domain. This band is located at 612 nm (f=1.817), in obviously good match with experimental values (see **Fig 4**). Theory predicts another absorption at longer wavelength (S_1, 810 nm) but with an oscillator strength that is 25 times smaller (f=0.073) which may explain the long tail at long wavelength seen experimentally (**Fig. 4**). Therefore, the presence of a shoulder-like peak in the experimental spectrum is attributed to vibronic couplings (not modelled here). The S_1 and S_3 state mainly correspond to a HOMO to LUMO and HOMO-1 to LUMO electronic promotions, respectively. These MOs are displayed in **Fig. S7** and are clearly delocalized over the full molecule.
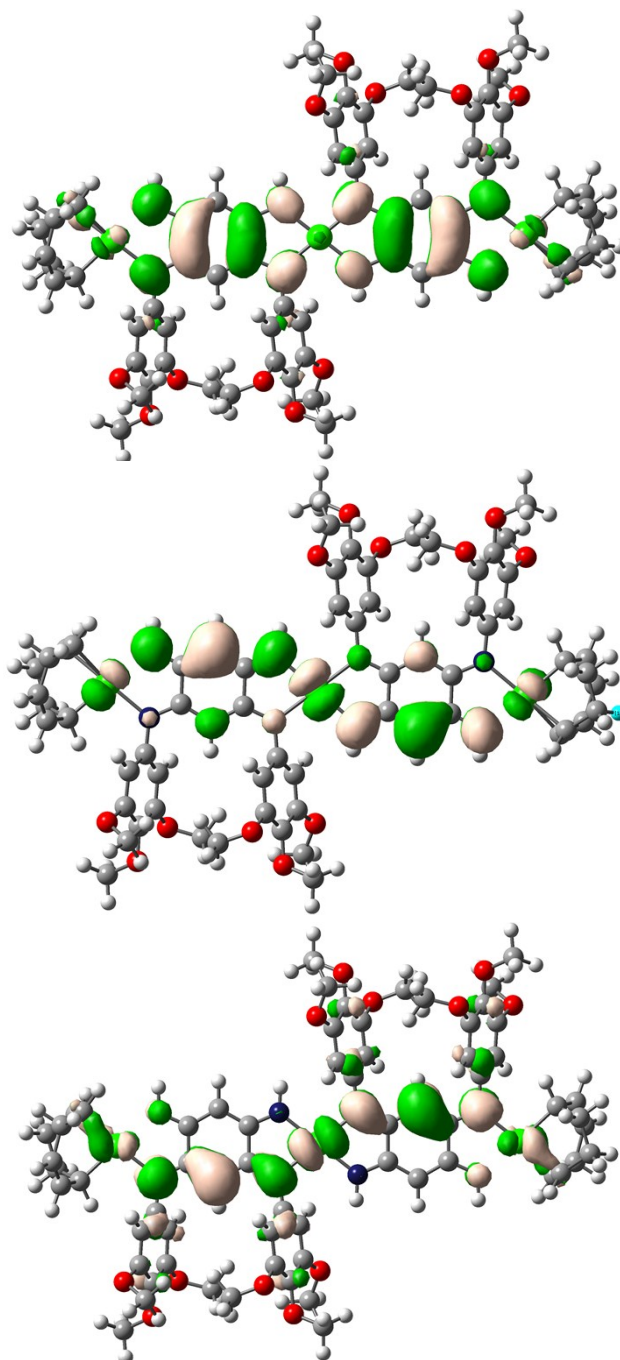
Figure S7. Frontier MOs of **14**. From top to bottom: LUMO, HOMO and HOMO-1 (contour: 0.02 au).

For the nickel-containing **15**, TD-DFT predicts a major absorption at 452 nm that can be mainly ascribed to a HOMO-1 to LUMO transition, the HOMO-LUMO band appearing at 599 nm but is nearly forbidden. The two key orbitals of **15** are displayed in **Fig. S8**. The occupied orbitals is highly delocalized on the central ligand, metal and acac groups whereas the unoccupied orbital is localized on the QDI only.
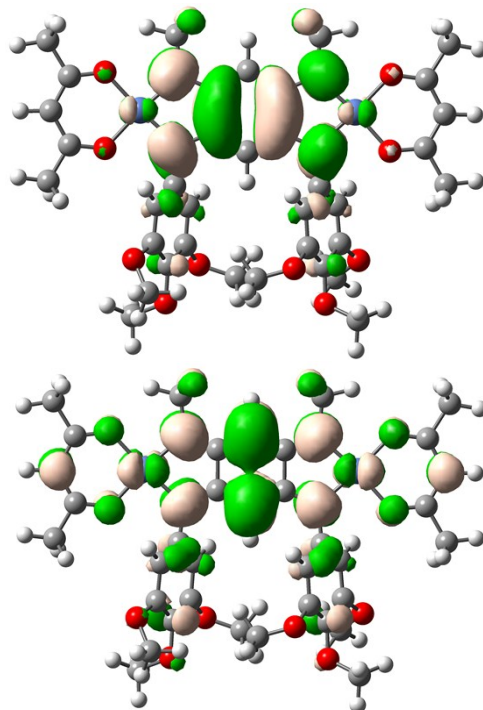
Figure S8. Frontier MOs of **15**. Top and bottom: LUMO and HOMO-1, respectively (contour: 0.02 au).

S3. Physico-Chemical Approach

S3a. Starting Materials and Solvents

Distilled water was further purified by passing it through a mixed bed of ion-exchanger (Bioblock Scientific R3-83002, M3-83006) and activated carbon (Bioblock Scientific ORC-83005) and was de-oxygenated by CO_2- and O_2-free argon (Sigma Oxiclear cartridge) before use. Spectrophotometric grade methanol (Merck, p.a.) and water were de-oxygenated by CO_2- and O_2-free argon (Sigma Oxiclear cartridge). All the stock solutions were prepared by weighing solid products using an AG 245 Mettler Toledo analytical balance (precision 0.01 mg). The ionic strength was maintained at 0.1 M with n-tetrabutylammonium perchlorate (NEt$_4$ClO$_4$, Fluka, puriss), and all measurements were carried out at 25.0(2) °C. *CAUTION! Perchlorate salts combined with organic ligands are potentially explosive and should be handled in small quantities and with the adequate precautions*.[9]

S3b. Absorption spectrophotometric titrations versus pH

Absorption spectrophotometric titrations of **2a** as a function of pH were performed to evaluate its acido-basic properties. For the sake of solubility, **2a** was dissolved in a mixed solvent made of 80% of methanol (Merck) and 20% of water by weight. Stock solutions of **2a** were

first prepared by quantitative dissolution of the corresponding solid samples in methanol. The **2a** solutions were then diluted in CH_3OH/H_2O solvent (80/20 by weight) containing the supporting electrolyte at 0.1 M (NBu_4ClO_4, Fluka, puriss). In a first set of absorption *vs.* pH titrations, an aliquot of 40 mL of **2a** solution was introduced into a jacketed cell (Metrohm) maintained at 25.0(2) °C by the flow of a Lauda E200 thermostat under argon atmosphere. The free hydrogen ion concentration was measured with a combined glass electrode (Metrohm 6.0234.500, Long Life) and an automatic titrator system 794 Basic Titrino (Metrohm) connected to a microcomputer (Tiamo light 1.2 program for the acquisition of the potentiometric data). The Ag/AgCl reference glass electrode was filled with NaCl (0.1 M, Fluka, p.a.) in CH_3OH/H_2O solvent (80/20 by weight). At an earlier stage, the combined glass electrode was calibrated as a hydrogen concentration probe by titrating known amounts of perchloric acid (~1.33×10^{-1} M from $HClO_4$, Prolabo, normapur, 70% min) with CO_2-free tetraethylammonium hydroxide solution (~1.10×10^{-1} M from Aldrich, purum, ~ 40 % in water).[10] The $HClO_4$ and NEt_4OH solutions were freshly prepared just before use in CH_3OH/H_2O solvent and their analytical concentrations were ascertained by colorimetric titrations with sodium tetraborate decahydrate ($B_4Na_2O_7.10H_2O$, Fluka, puriss, p.a.) and potassium hydrogen phthalate ($C_8H_5KO_3$, Fluka, puriss, p.a.), respectively, using methyl orange (RAL) and phenolphthalein (Prolabo, purum) as the indicators. The GLEE program was applied for the glass electrode calibration and to check carbonate levels of the NEt_4OH solutions used (< 5%). The initial pH of the **2a** solution was adjusted to ~ 2 with $HClO_4$ (Prolabo, normapur, 70% min), and duplicated titrations of **2a** (~2 < pH < ~11.7) were then carried out (**Fig. S8** and **Fig. S9**) by addition of known volumes of NEt_4OH solutions using the automatic titrator of the 794 Basic Titrino device. After each addition, an absorption spectra was repeatedly recorded using a Varian CARY 50 spectrophotometer fitted with Hellma optical fibers (Hellma, 041.002-UV) and an immersion probe made of quartz suprazil (Hellma, 661.500-QX) and interfaced (Cetrib) with the potentiometric unit. In a second set of absorption *vs.* pH titrations, 40 µL of a methanolic **2a** stock solution (3.05×10^{-3} M) was introduced into a 1 cm Hellma optical cell made of quartz Suprasil containing 1 mL of the CH_3OH/H_2O solvent (80/20 by weight) at 0.1 M of the supporting electrolyte (NBu_4ClO_4, Fluka, puriss). The pH was gradually decreased to very acidic values by adding known volumes of $HClO_4$ (from $HClO_4$, Prolabo, normapur, 70% min) with an Eppendorf microburette. The $HClO_4$ concentrations were converted into a pH scale. After each addition, an absorption spectrum was recorded using a UV-Vis.-NIR Varian CARY 5000 spectrophotometer (**Fig. S10**).

The volume and thereby the pH increments along the absorption versus pH titrations are automatically adjusted by the potentiometric system according the signal drift of the solution. The DET (dynamic Potential Titration) method of the Tiamo program was used with a measuring point density of 3.

S3c. Analysis and processing of the spectroscopic data

The spectrophotometric data were analysed with Specfit[11] suite of programs that adjusts the absorptivities and the stability constants of the species formed at equilibrium. Specfit uses factor analysis to reduce the absorbance matrix and to extract the eigenvalues prior to the multi-wavelength fit of the reduced data set according to the Marquardt algorithm.[12,13] The distribution curves of the protonated species of **2a** as a function of pH were calculated using the Hyss program (**Fig. S11**).[14]
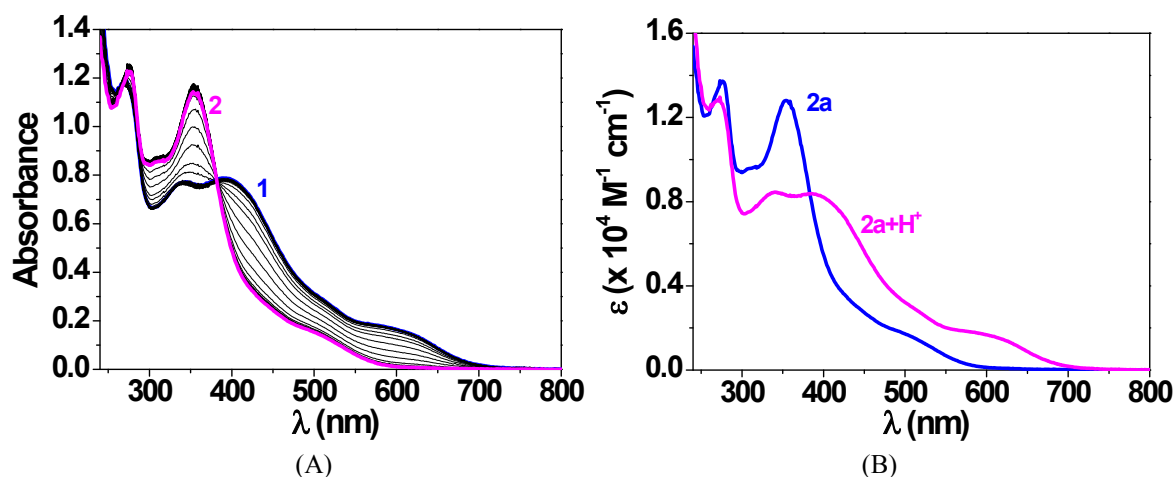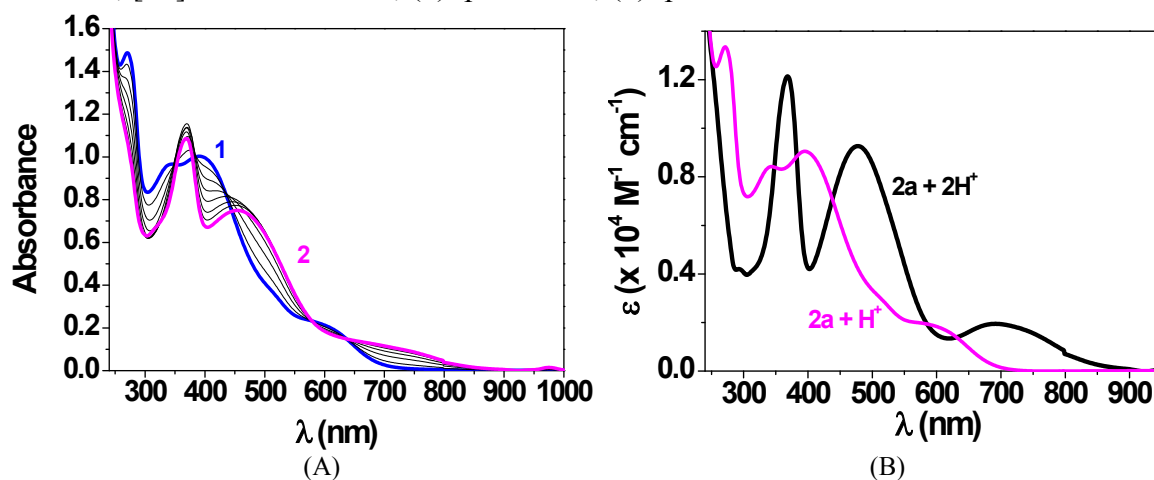
Fig. S9. (A) Absorption *versus* pH titration of **2a**. (B) Electronic absorption spectra of **2a** and its monoprotonated species. Solvent: CH_3OH/H_2O (80/20 *w/w*); I = 0.1 M (NBu_4ClO_4); T = 25.0°C; [**2a**] = 9.24 × 10^{-5} M; (1): pH = 2.83; (2) : pH = 11.74.
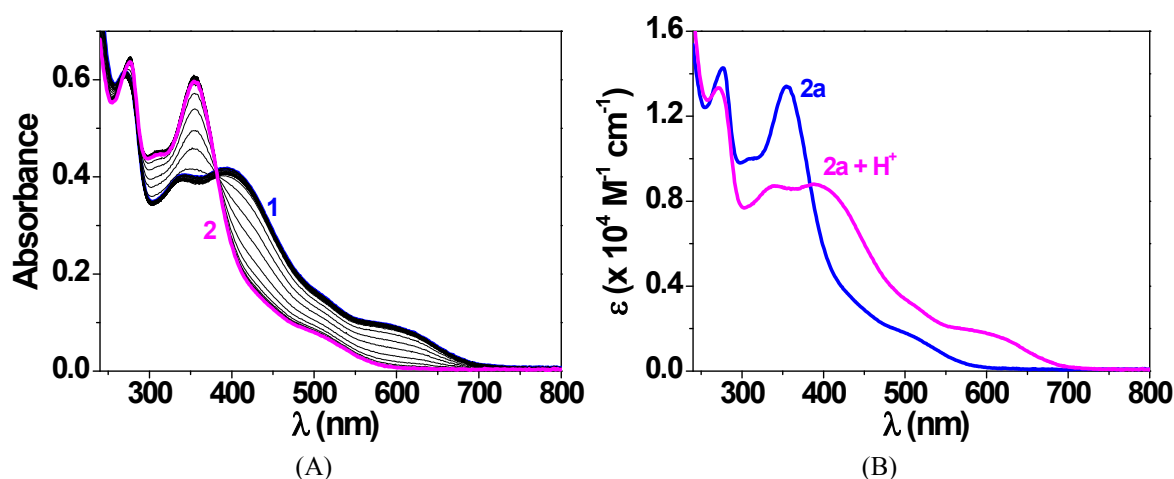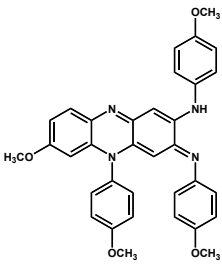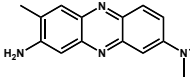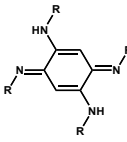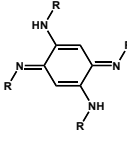

Fig. S10. (A) Absorption *versus* pH titration of **2a**. (B) Electronic absorption spectra of **2a** and its monoprotonated species. Solvent: CH_3OH/H_2O (80/20 *w/w*); I = 0.1 M (NBu_4ClO_4); T = 25.0°C; [**2a**] = 4.61 × 10^{-5} M; (1): pH = 2.71; (2): pH = 11.61.
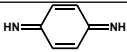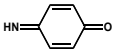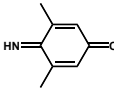
Fig. S11. (A) Absorption *versus* pH titration of **2a**. (B) Electronic absorption spectra of the mono- (**2a·H⁺**) and diprotonated species (**2a·2H⁺**) of **2a**. Solvent: CH_3OH/H_2O (80/20 *w/w*); I = 0.1 M (NBu_4ClO_4); T = 25.0°C; [**2a**] = 1.17 × 10^{-4} M; (1): pH = 1.64; (2): pH = 0.24.
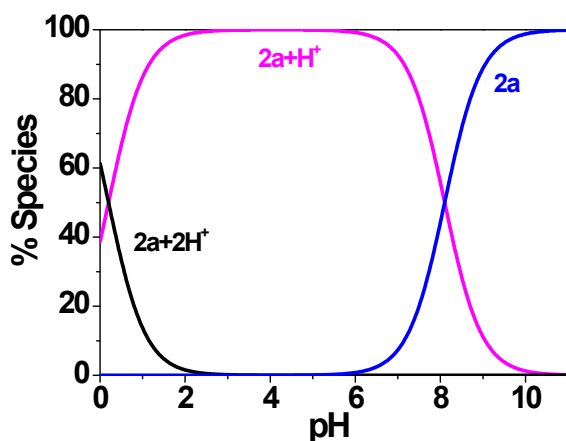
Fig. S12. Distribution diagrams of the protonated species of 2a as a function of pH; $T =$ 25.0°C; $[\mathbf{2a}] = 10^{-4}$ M; (1): pH = -1 ; (2): pH = 11.

Table S1. Protonation constants of related quinone-imine and quinone-diimine derivatives.

compound	pK_{a1}	pK_{a2}	ΔpK_a	Solvent	ref
	~3	5.75	~2.75	H_2O	15
	3.72(6)		na	H_2O	16
	3.06(3)		na	H_2O	16
	6.6(2)		nd	CH_3CN/H_2O (70/30 v/v)	17
Neutral red	7.35			water	18
R = *neo*-pentyl	5.75(2)	8.28(2)	2.53	CH_3OH/H_2O (80/20 w/w)	19
R = benzyl	5.80(7)	7.96(5)	2.16	CH_3OH/H_2O (80/20 w/w)	19

S4. Experimental general information

All reagents and solvents were purchased from Alfa Aesar or Sigma Aldrich and were used without further purification. Column chromatography was performed using silica gel (60-120 mesh). Analytical thin layer chromatography (TLC) was performed on precoated silica gel-60 F254 (0.5 mm) aluminium plate. Visualization of the spots on TLC plates was achieved by exposure to UV light. Size exclusion chromatography was performed on Bio-Beads S-X3 Resin.

^{1}H NMR spectra were recorded on ECS400 Jeol spectrometer operating 400 MHz. ^{13}C NMR spectra were recorded on ECS400 Jeol spectrometer 100 MHz. ^{13}C solid state NMR are recorded on Bruker Avance III WB 400 MHz. Chemical shifts are reported in delta (δ) units, expressed in parts per million using the residual protonated solvent as an internal standard (For proton: $CDCl_3$, 7.26 ppm; DMSO-d_6, 2.50 ppm; CD_2Cl_2, 5.32 ppm. For ^{13}C: $CDCl_3$, 77.0 ppm; DMSO-d_6, 39.4 ppm). The multiplicity of signals is designated by the following abbreviations: s, singulet; br s, broad singulet; d, doublet; t, triplet; br t, broad triplet; q, quartet; quint, apparent quintet; sext, apparent sextet; m, multiplet. Coupling constants, *J*, are reported in Hertz (Hz). High Resolution Mass Spectrometry (HRMS-ESI) and Mass Spectrometry (ESI-MS) analyses were performed on a QStar Elite (Applied Biosystems SCIEX) spectrometer or on a SYNAPT G2 HDMS (Waters) spectrometer. These two instruments are equipped with an electrospray ionization source or a matrix-assisted laser desorption/ionization source. Elemental analyses were determined with a Thermo Finnigan EA 1112.

For compounds of type **7** and **2,** no ^{13}C NMR spectra could be recorded owing to their poor stability in solution, and problem of relaxation (well known for this class of compounds), respectively.

S5. NMR data

* indicates the presence of solvent, grease or water
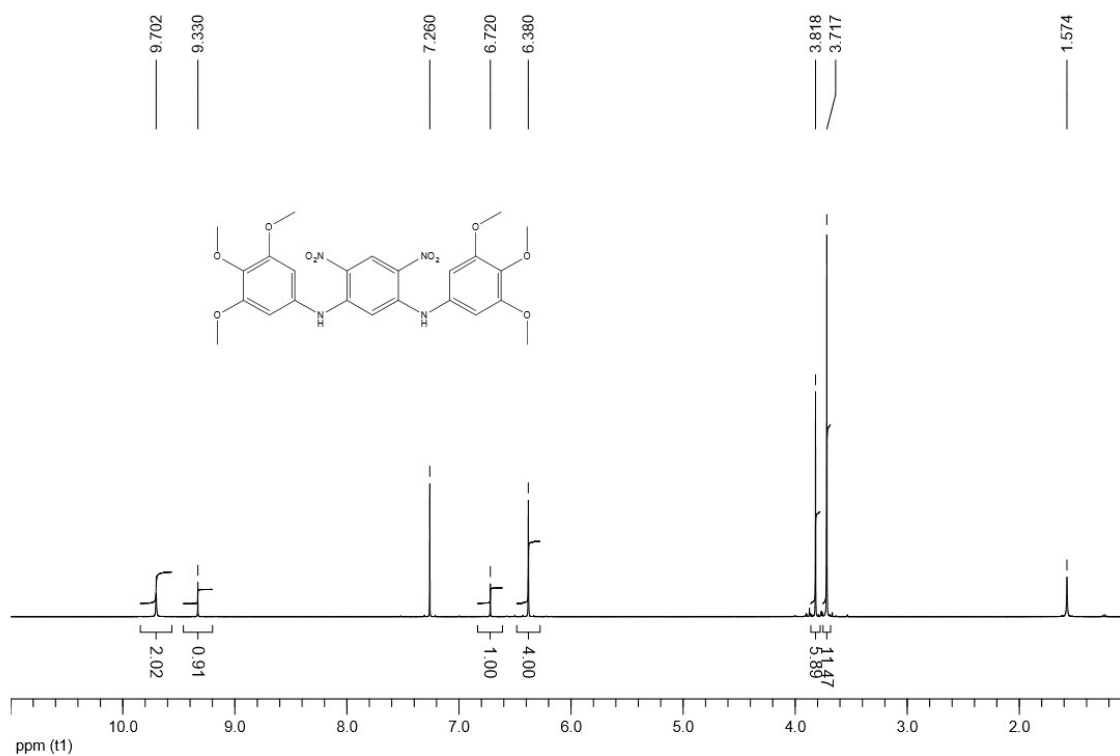
Fig. S13. ^{1}H NMR of **7a** in CDCl$_3$.
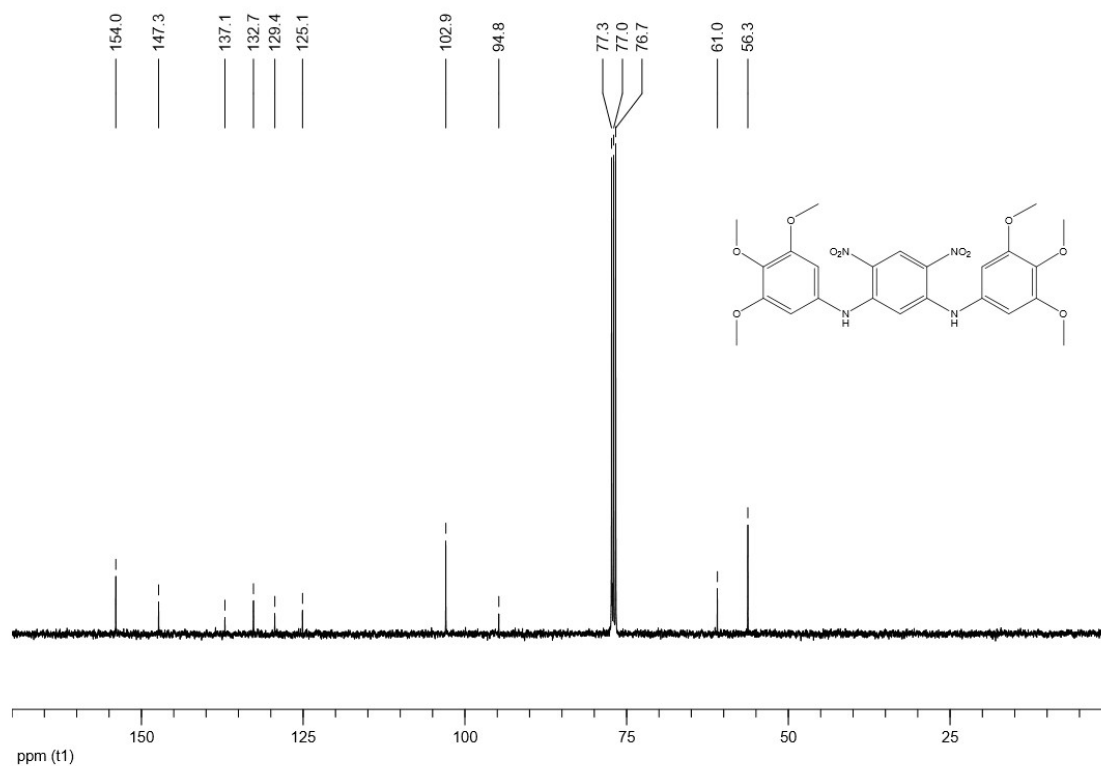
Fig. S14. ^{13}C NMR of **7a** in CDCl$_3$.
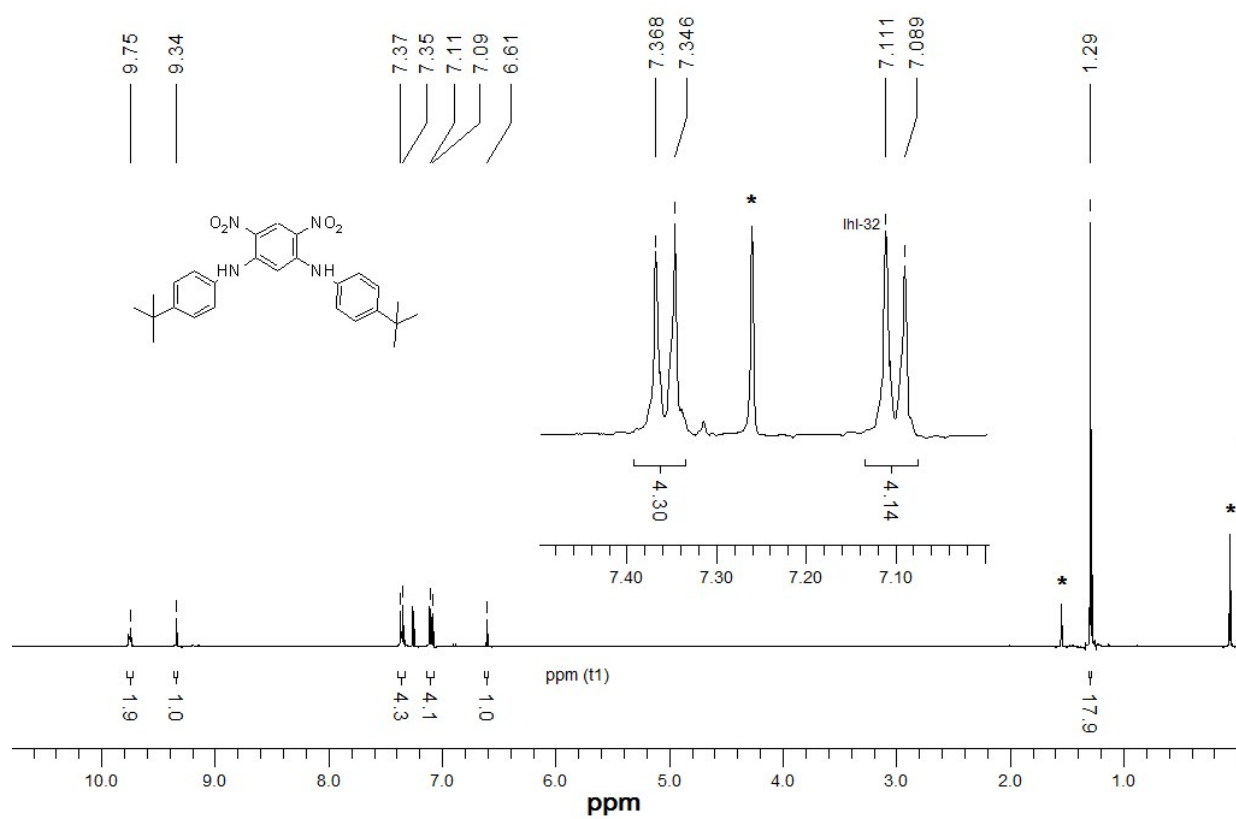
Fig. S15. ^{1}H NMR of **7b** in CDCl$_3$.
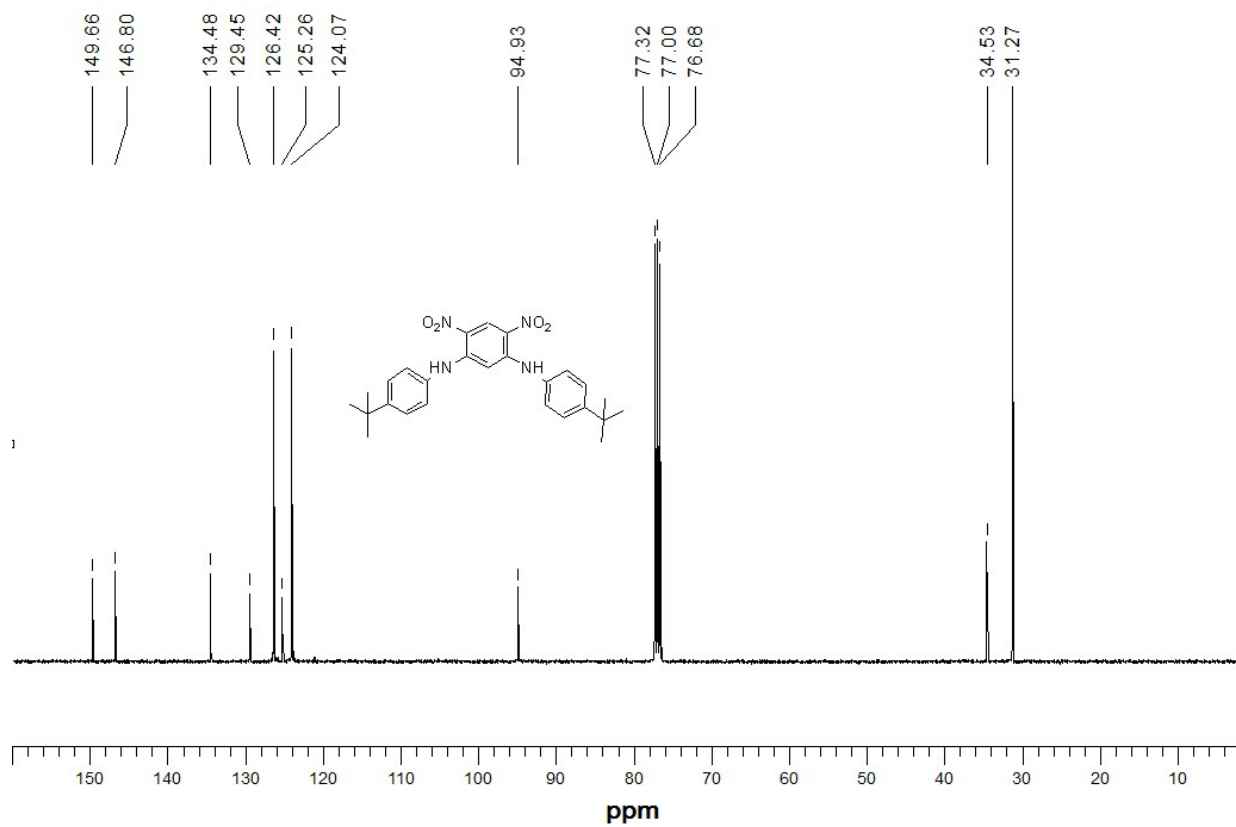
Fig. S16. ^{13}C NMR of **7b** in CDCl$_3$.
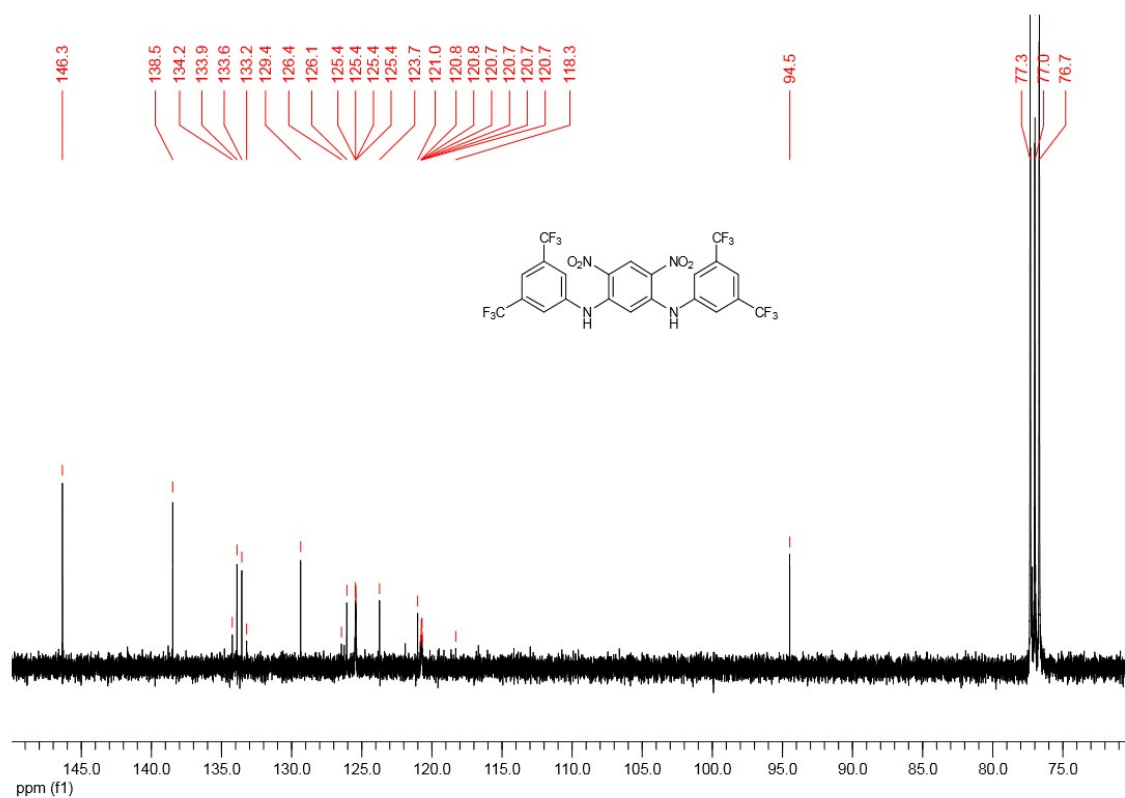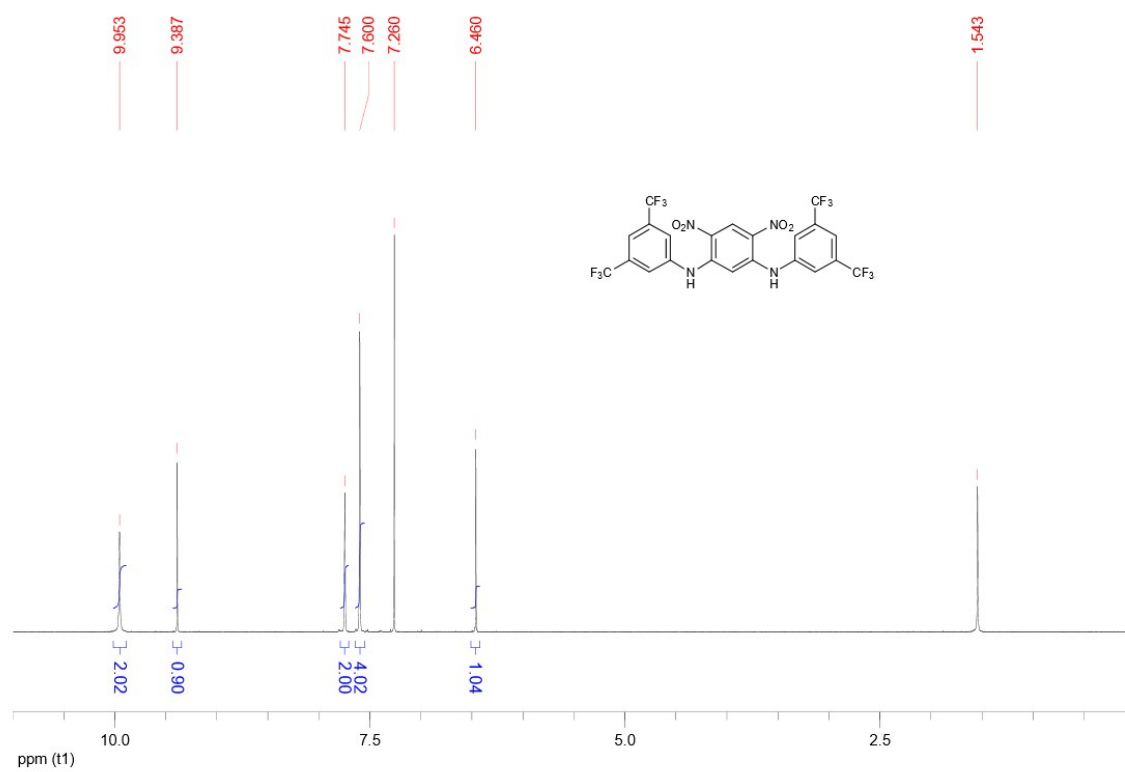
Fig. S17. ^{1}H (top) and ^{13}C NMR (bottom) of **7c** in CDCl$_3$.
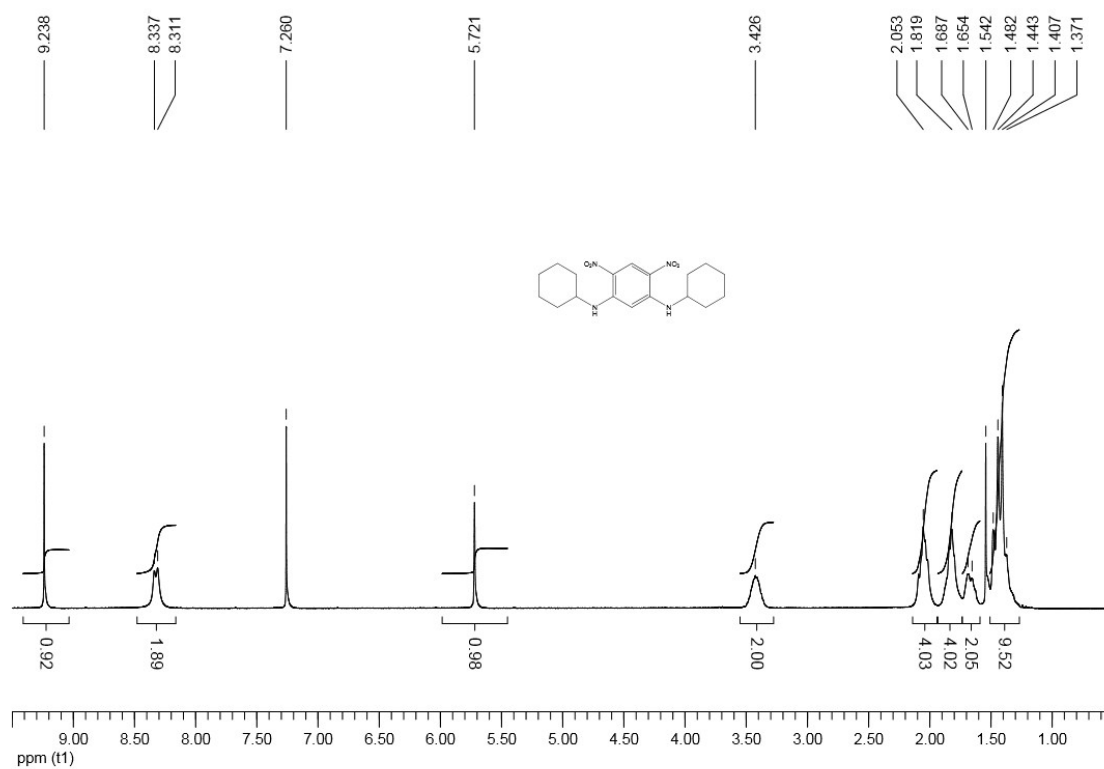
Fig. S18. ^{1}H NMR of **7d** in CDCl$_3$.
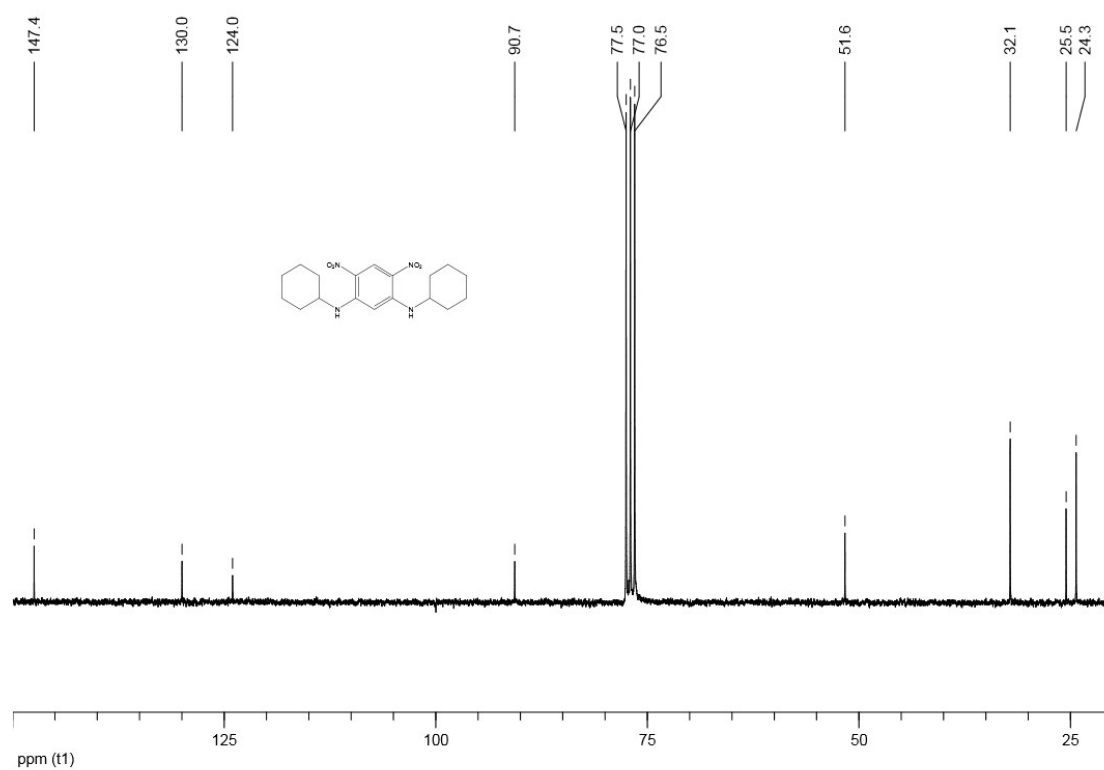
Fig. S19. ^{13}C NMR of **7d** in CDCl$_3$.
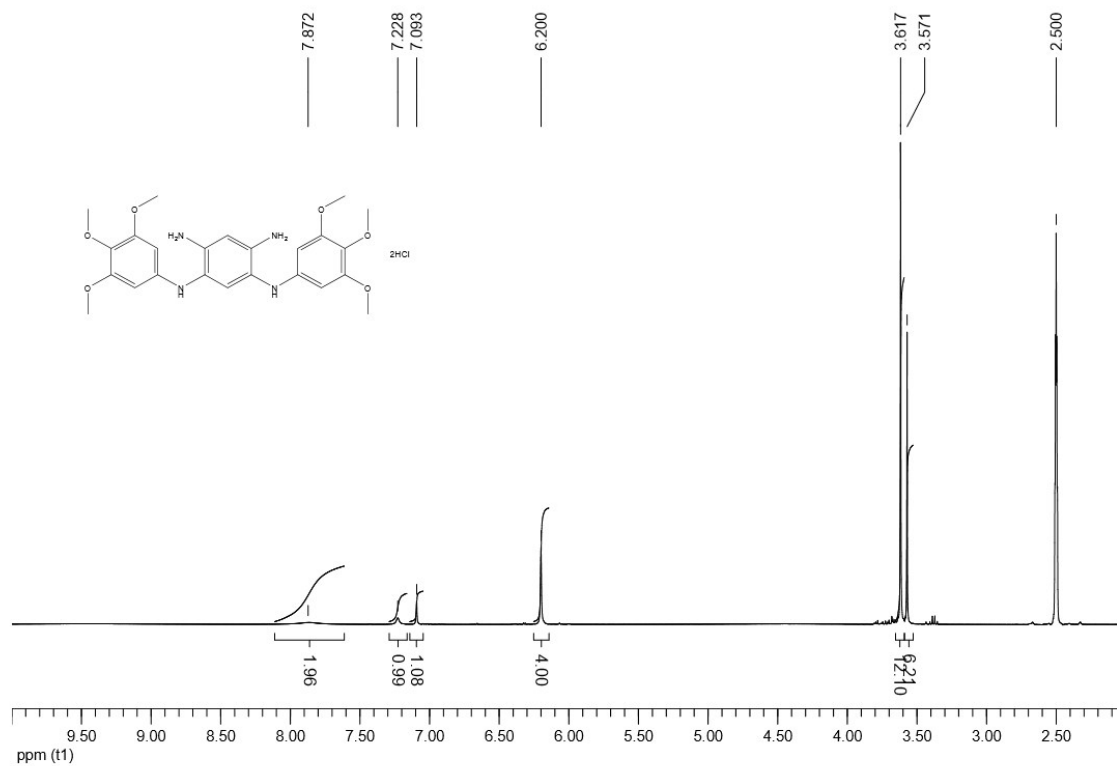
Fig. S20. ^{1}H NMR of **8a** in DMSO-d$_6$.
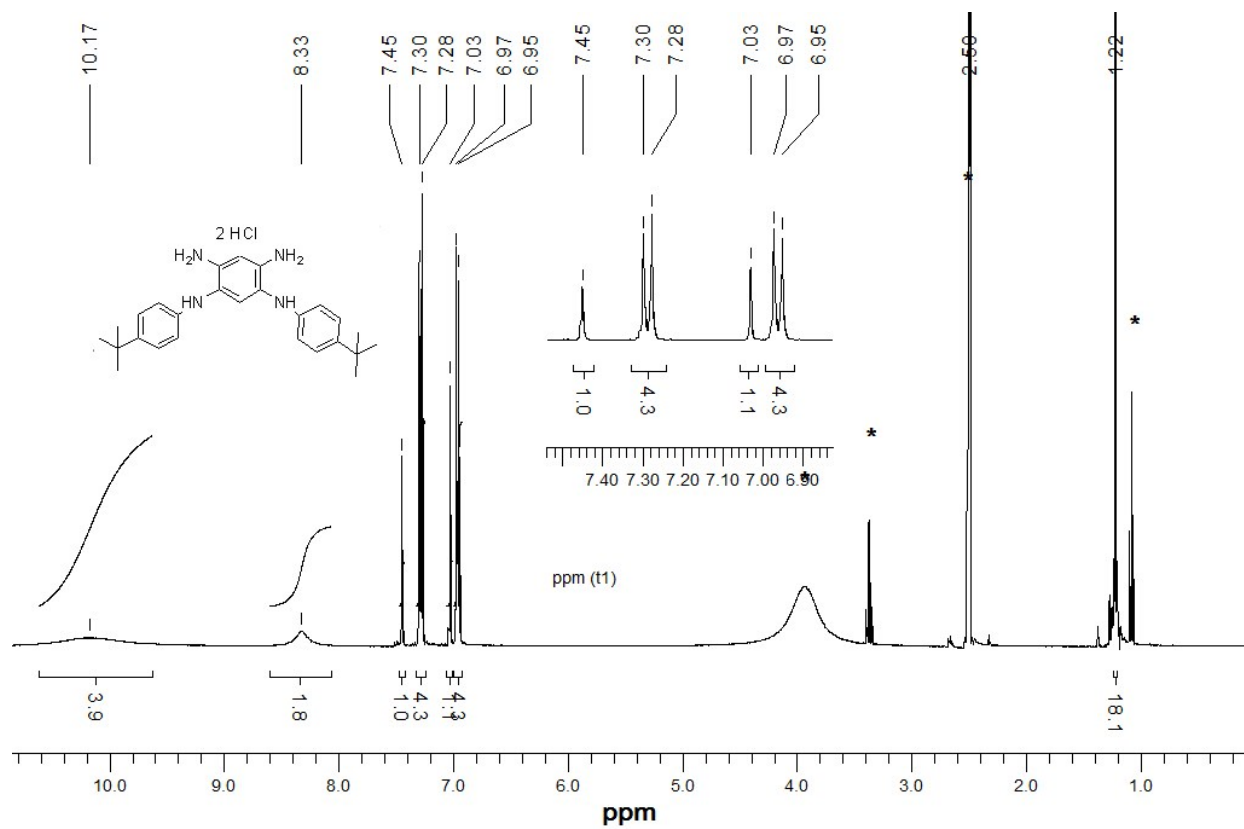
Fig. S21. ^{1}H NMR of **8b** in DMSO-d$_6$.

16
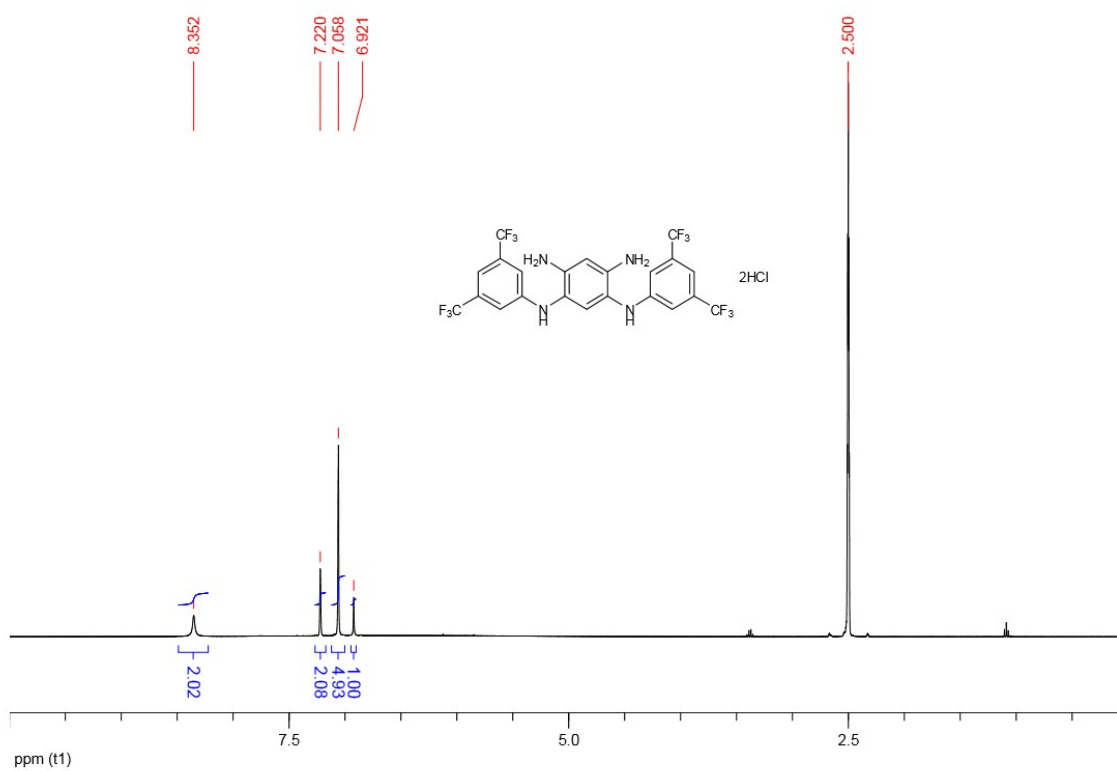
Fig. S22. ^{1}H NMR of **8c** in DMSO-d$_6$.
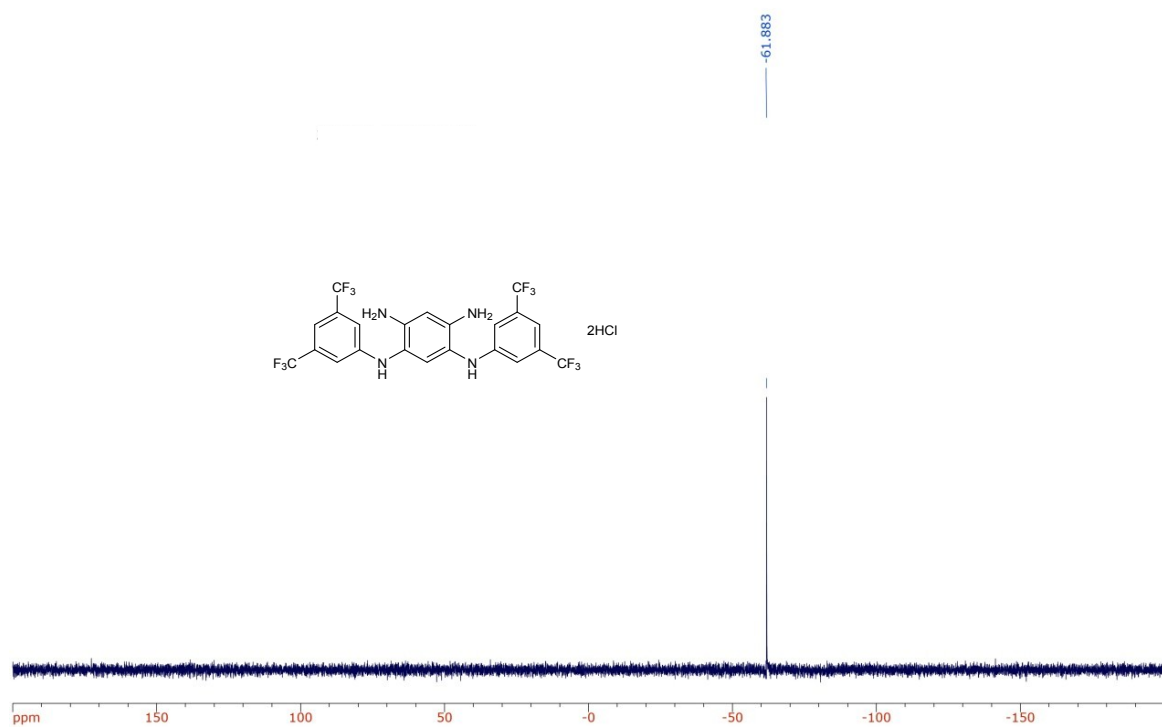
Fig. S23. ^{19}F NMR of **8c** in DMSO-d$_6$.
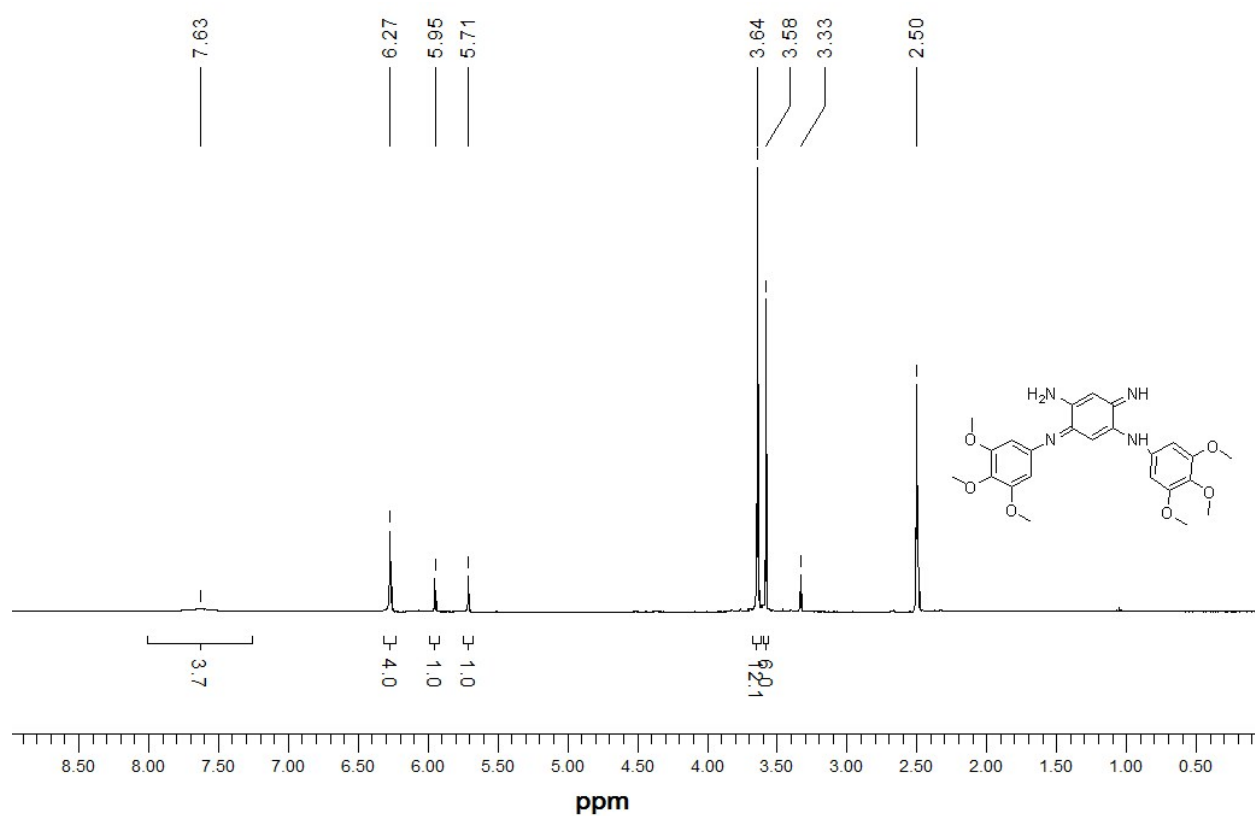
Fig. S24. ^{1}H NMR of **2a** in DMSO-d$_6$.
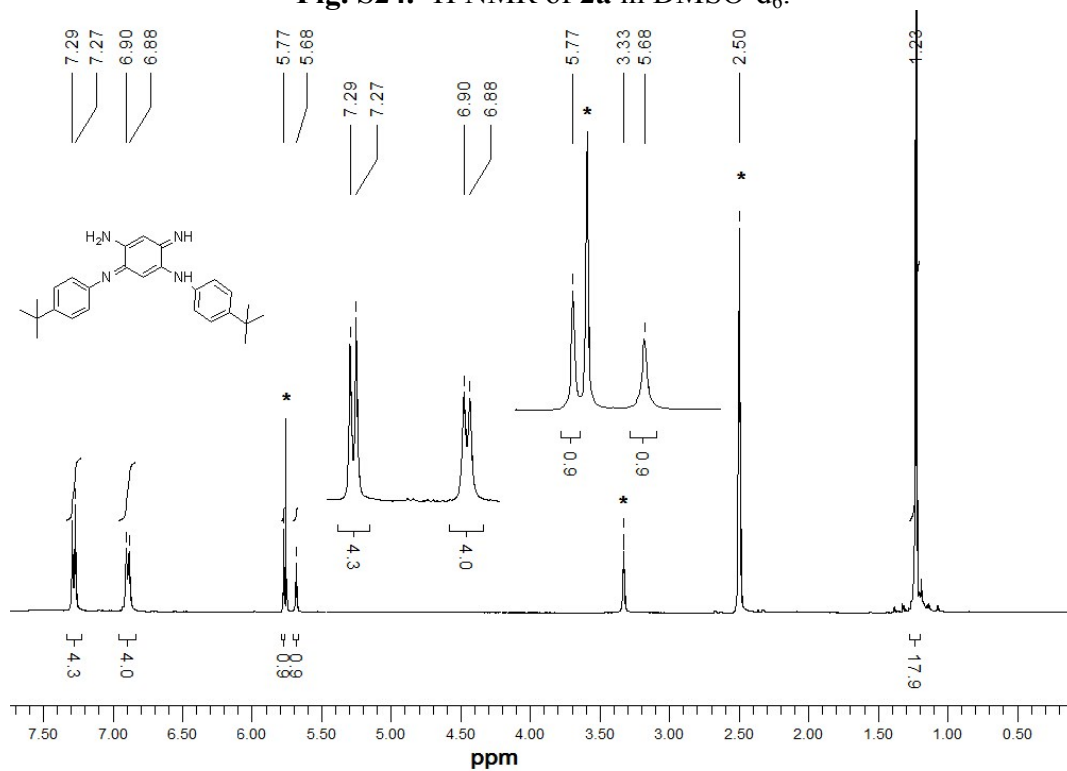
Fig. S25. ^{1}H NMR of **2b** in DMSO-d$_6$.

18

Fig. S26. ^{1}H NMR of **2c** in CDCl$_3$.

Fig. S27. ^{1}H NMR of **2d** in DMSO-d$_6$.
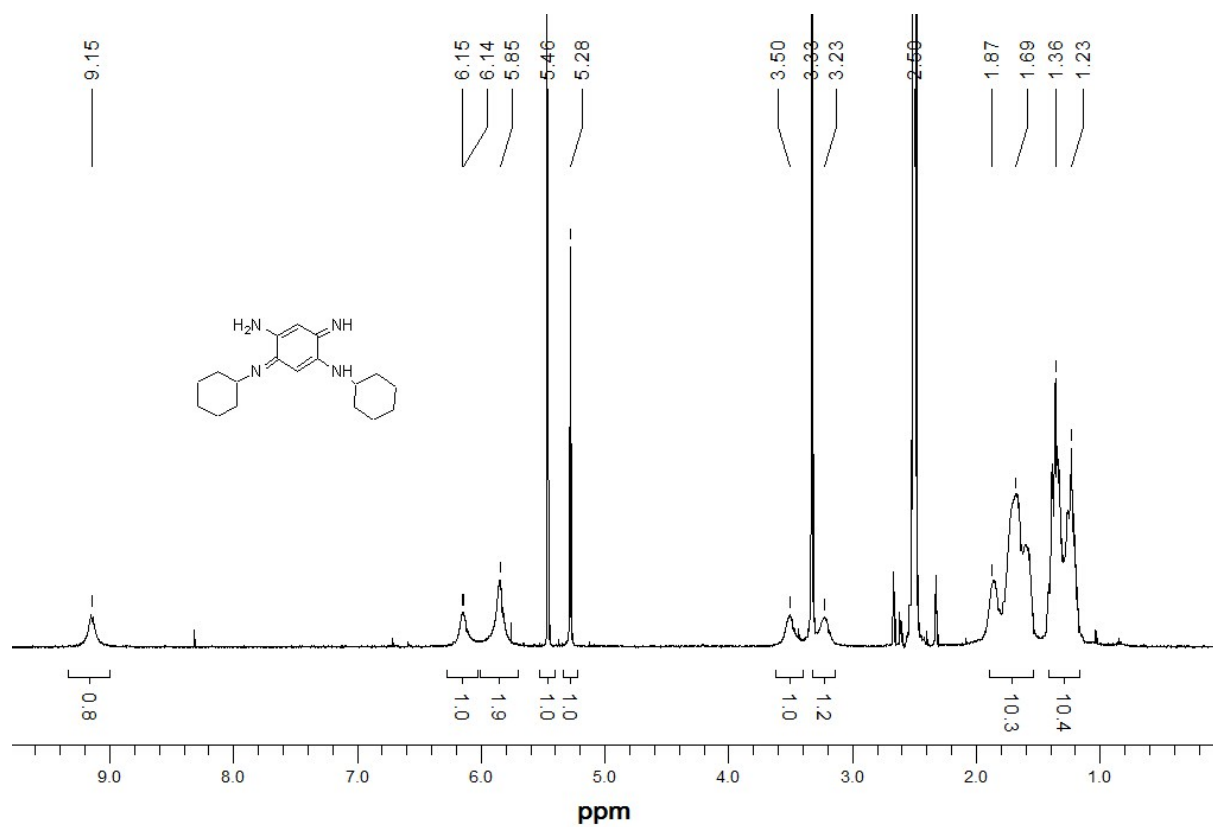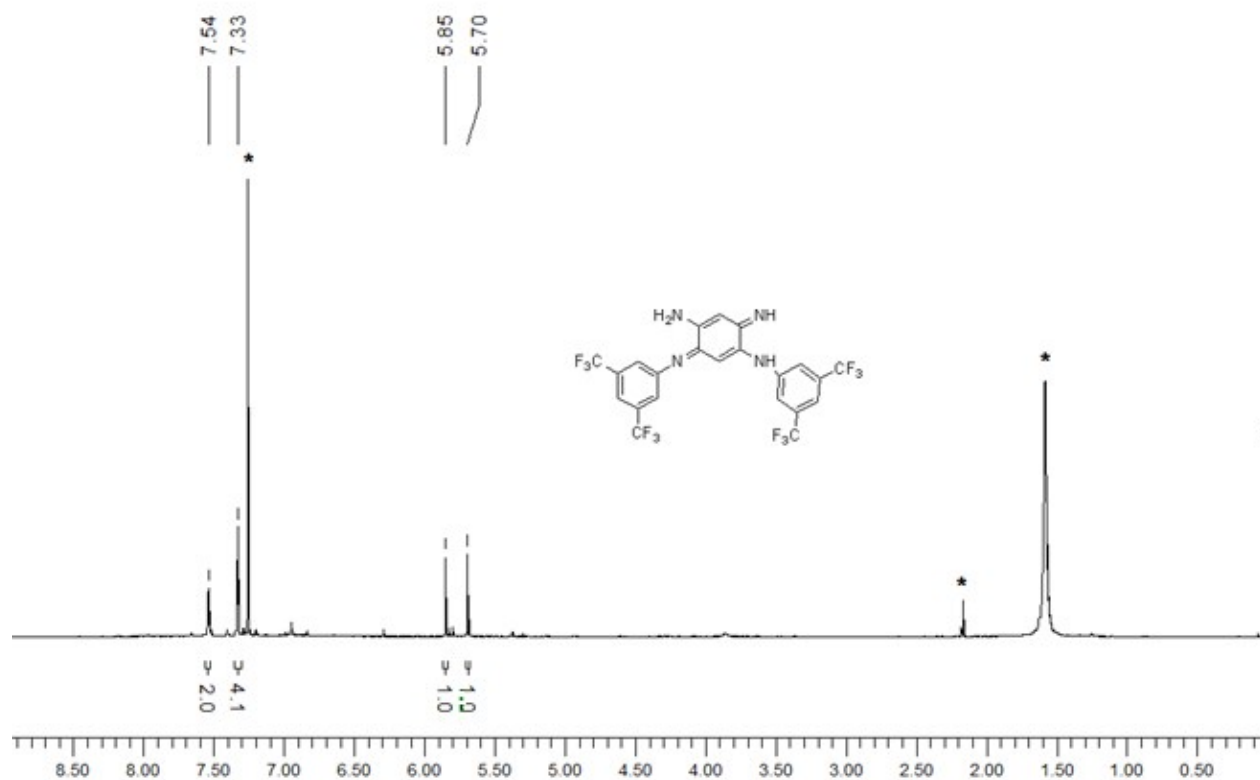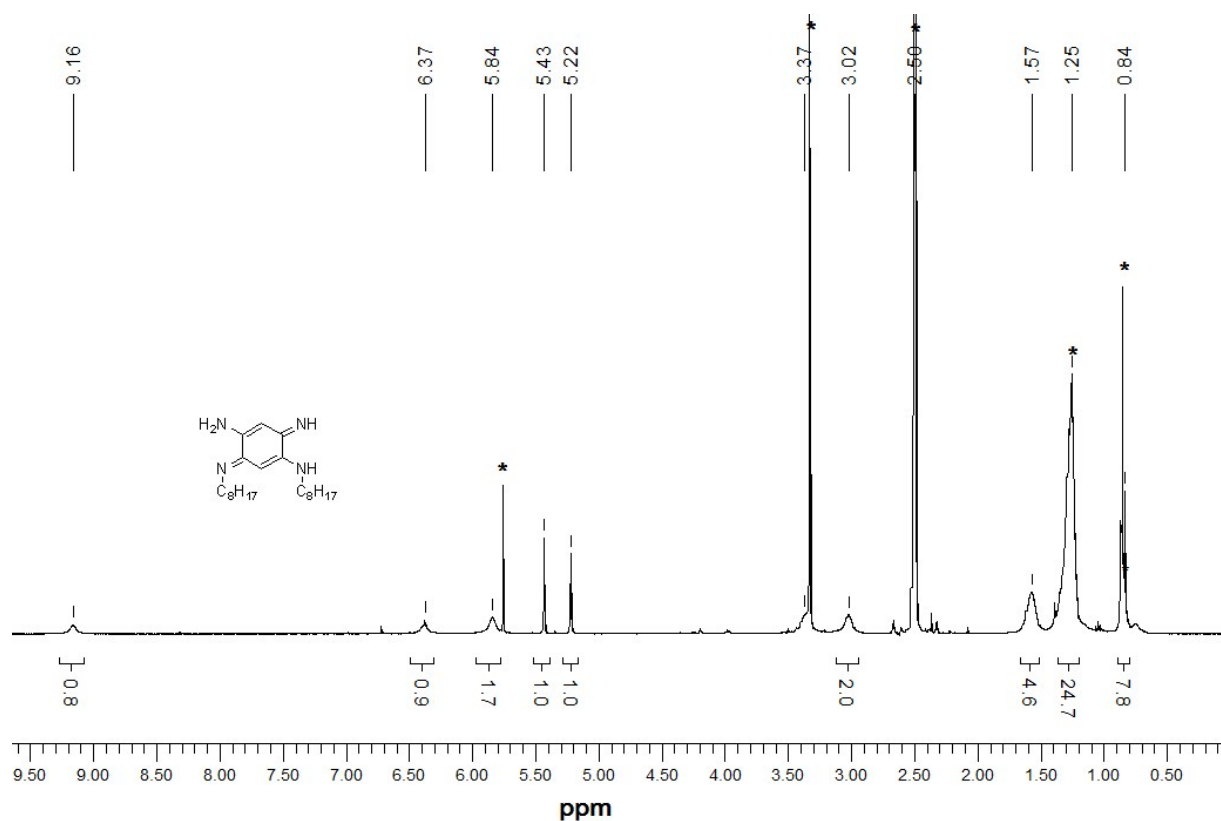
Fig. S28. ^{1}H NMR of **2e** in DMSO.
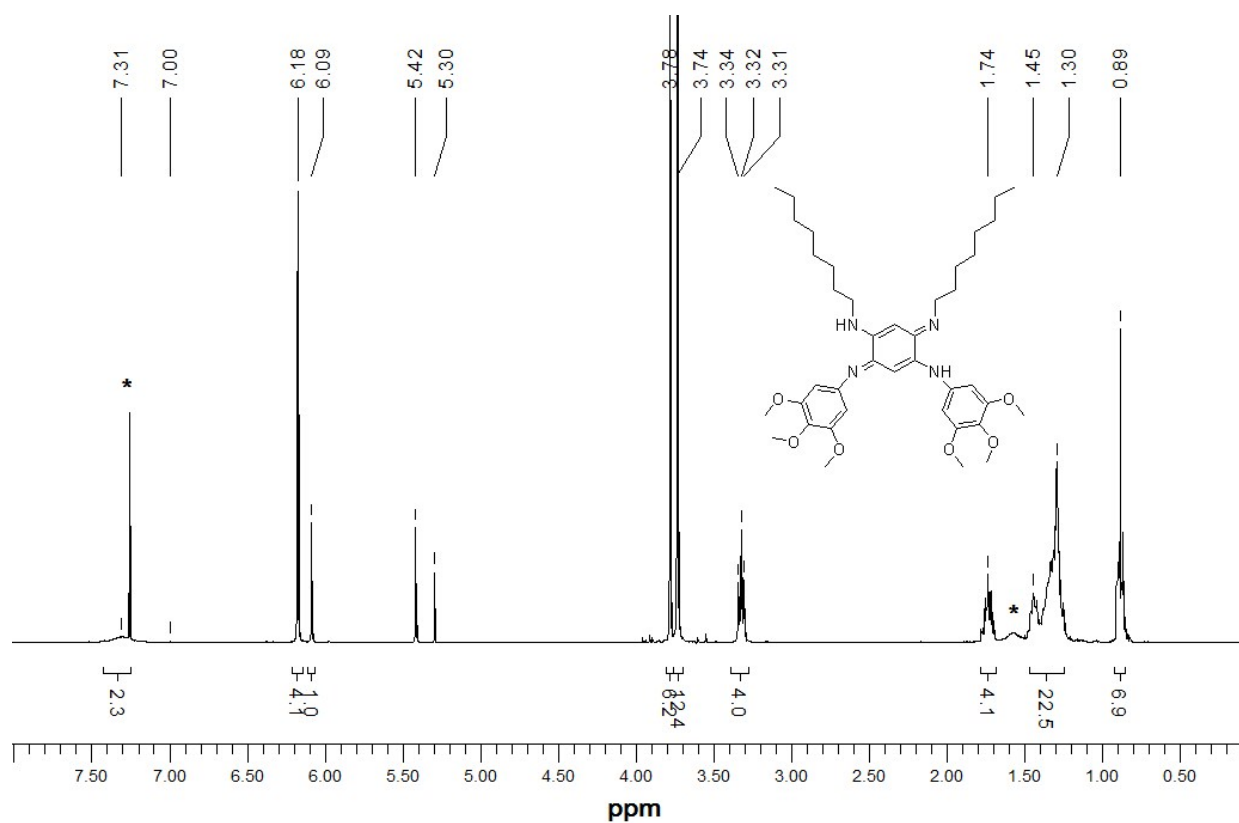
Fig. S29. ^{1}H NMR of **4a** in CDCl$_3$.
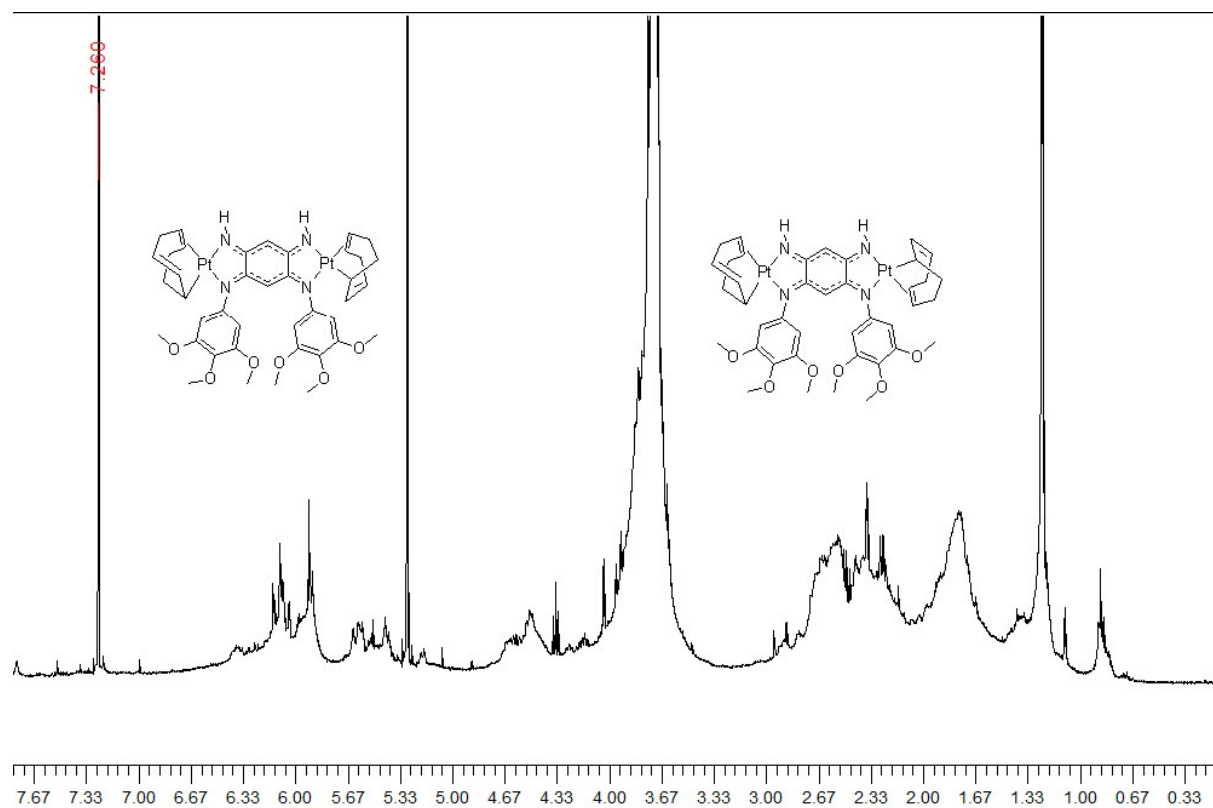
Fig. S30. ^{1}H NMR of **12** in CDCl$_3$.
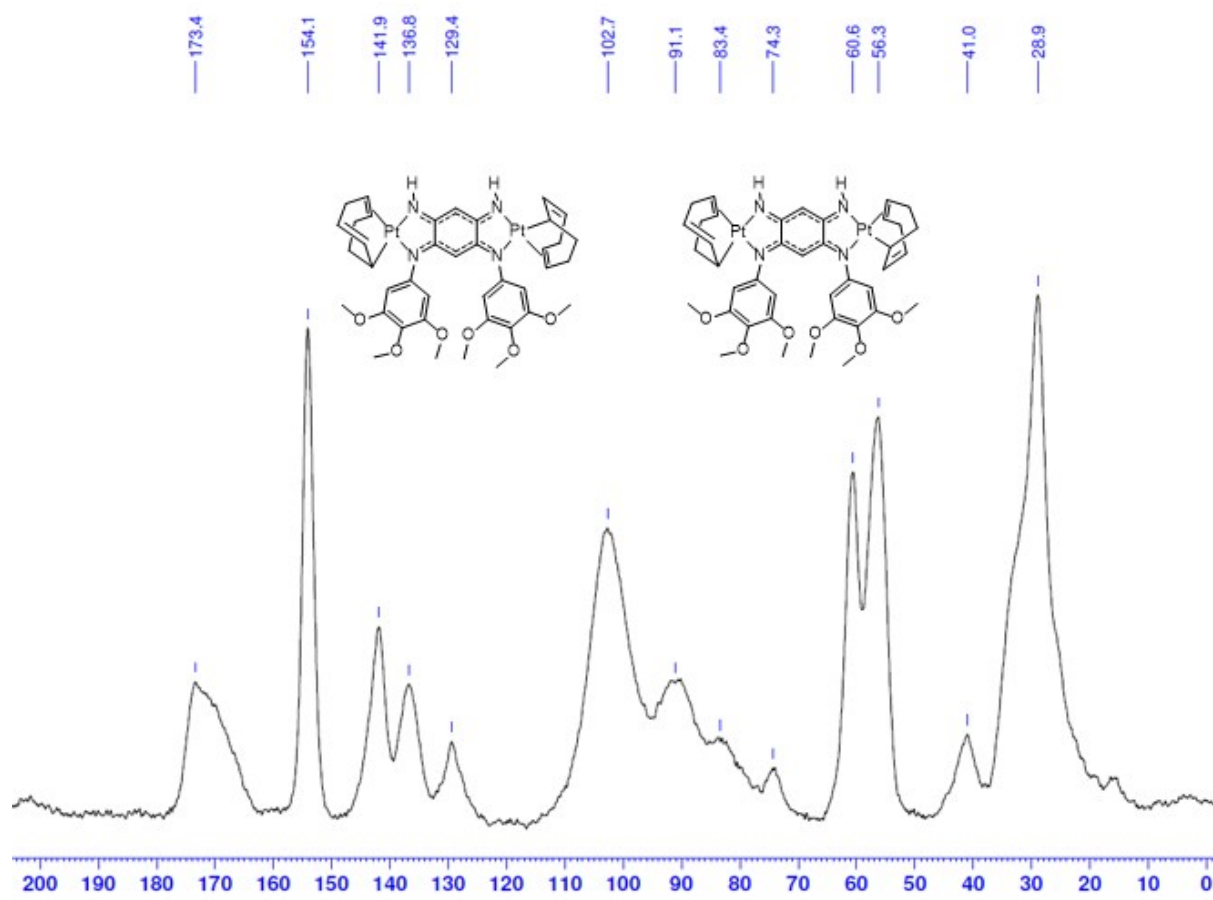
Fig. S31. ^{13}C solid state NMR of **12** in CDCl$_3$.
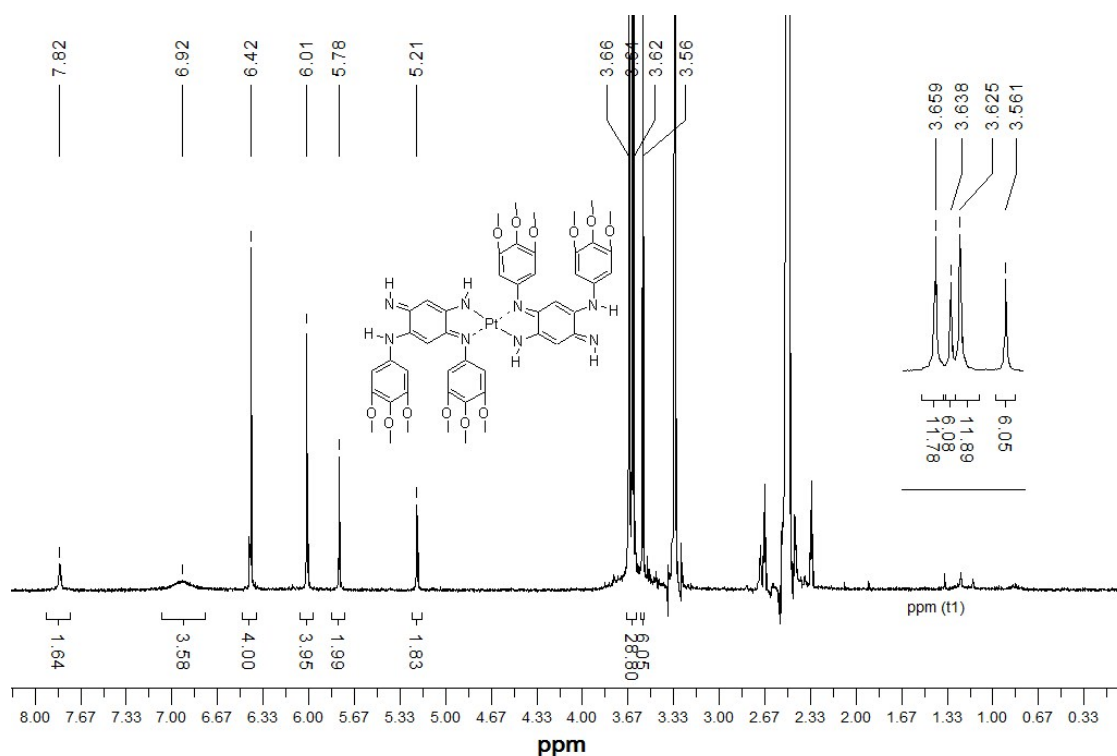
Fig. S32. ^{1}H NMR of **13** in DMSO-d$_6$.
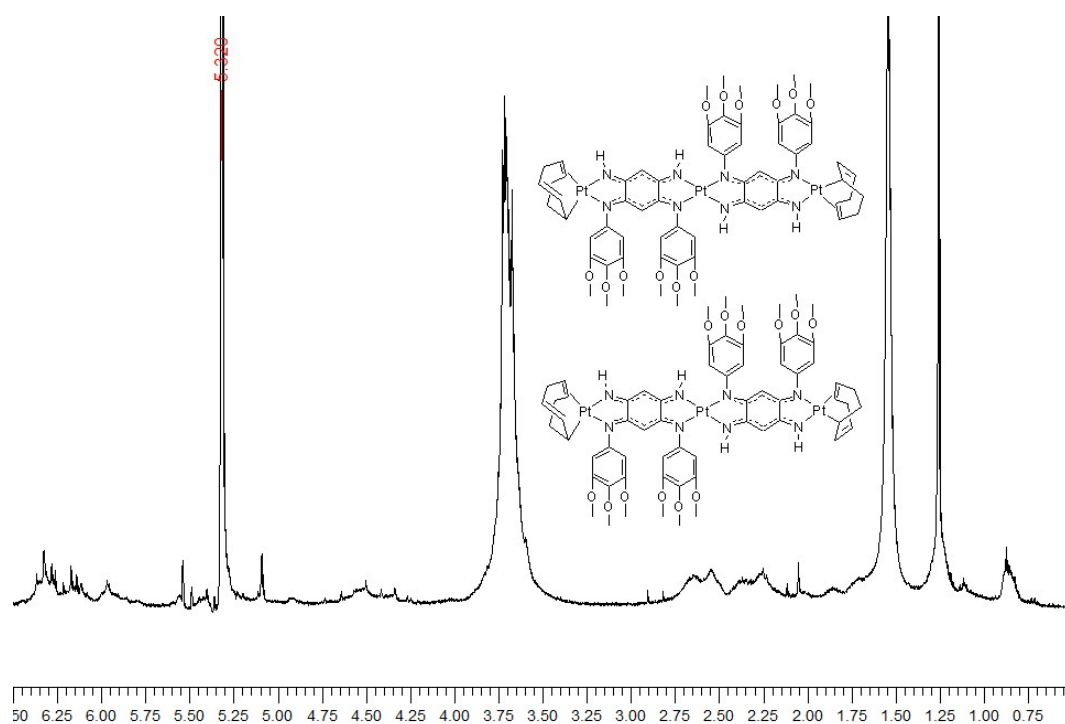
Fig. S33. ^{1}H NMR of **14** in CD$_2$Cl$_2$.

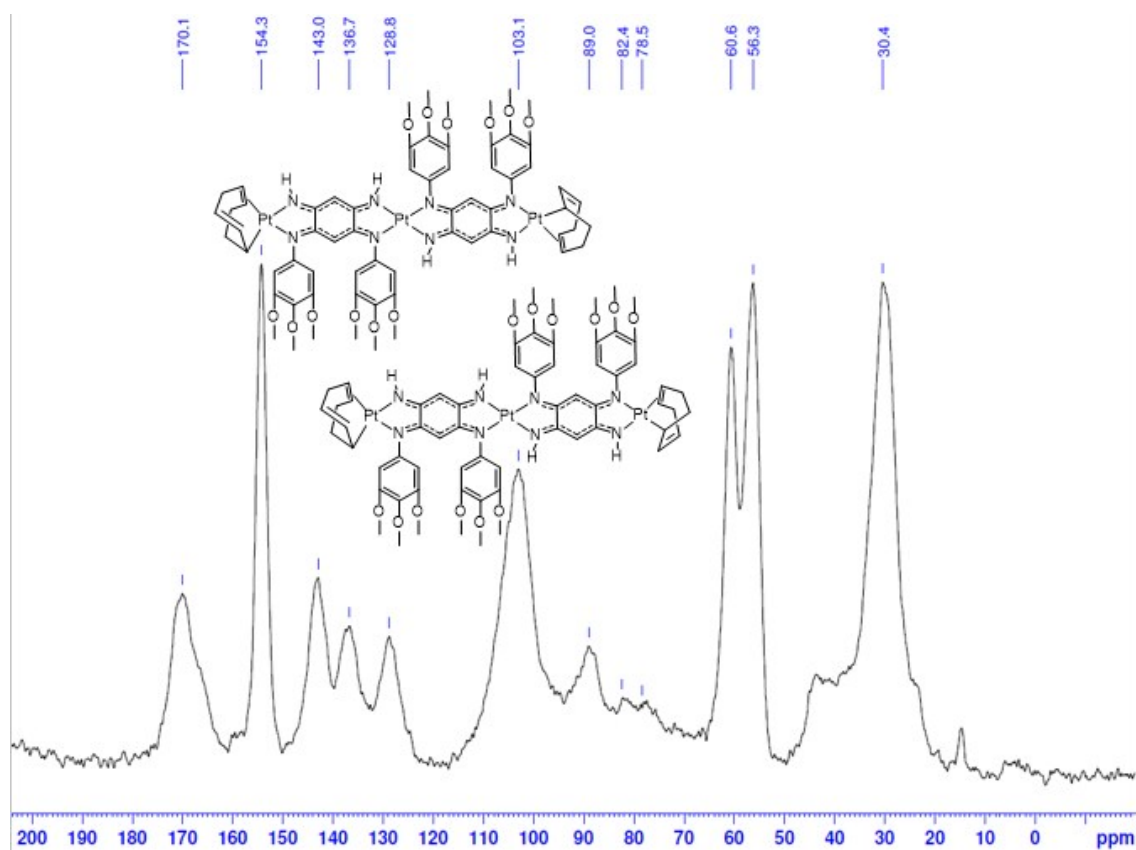**Fig. S34.** ^{13}C solid state NMR of **14** in CDCl$_3$

NMR spectra of **12** and **14** appeared poorly workable probably due to the presence of two isomers in solution, or the possible different hapticity of the cod ligands.
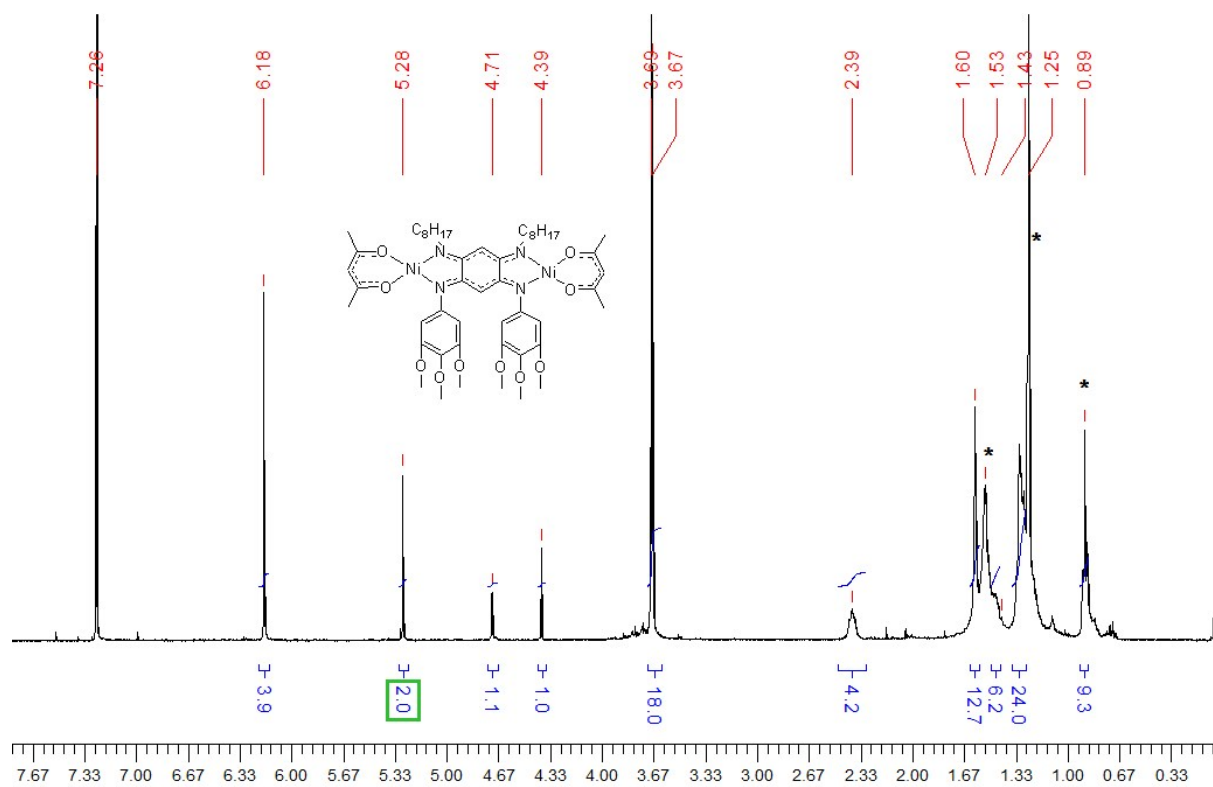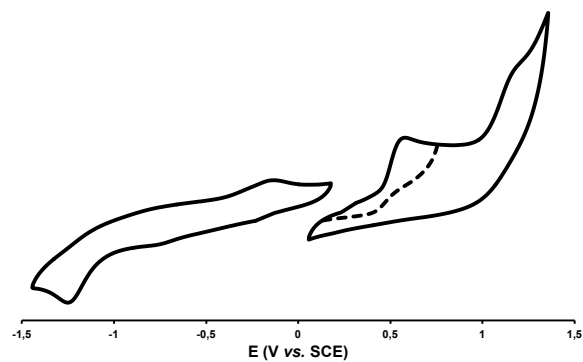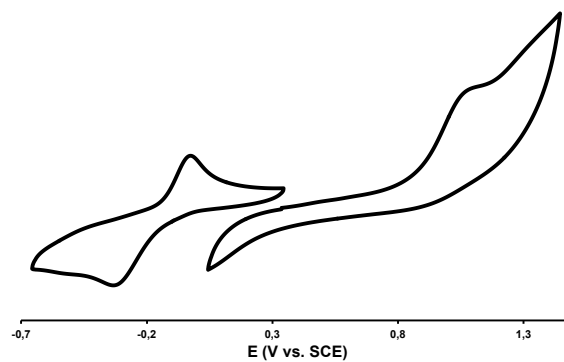
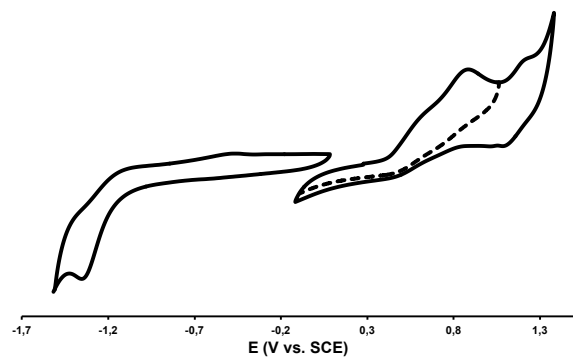

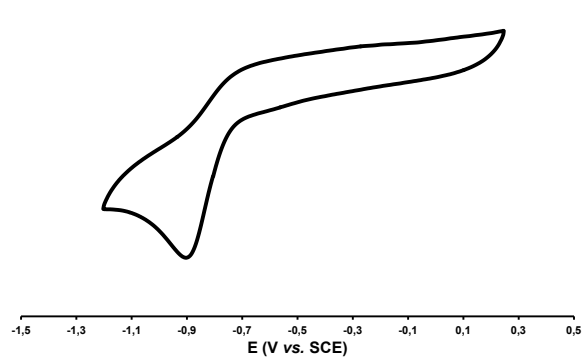**Fig. S35.** ^{1}H NMR of **15** in CDCl$_3$.

S6. Electrochemical studies
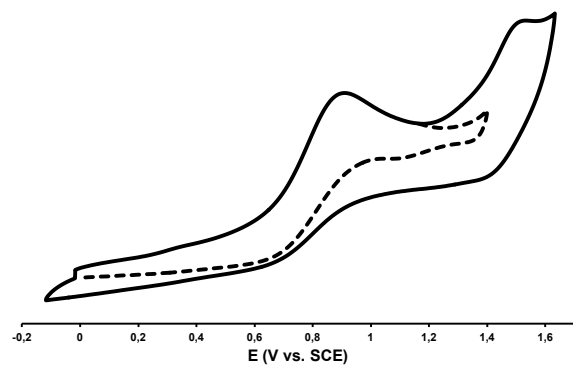
a) **2a**

b) **2a-HPF6**

c) **2b**

d) **2c**

e) **2d**

f) **2e**
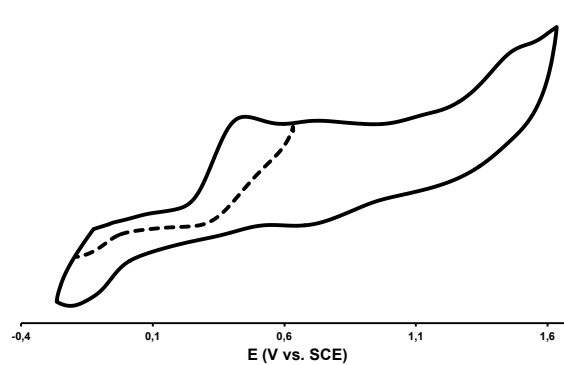
Fig. S36: Cyclic Voltammograms of **2a-e** and **2a-HPF$_6$** in CH$_2$Cl$_2$ containing 0.1 M of [(nBu$_4$N)PF$_6$] at room temperature with a scan rate of 100 mV/s.

a) **4a**
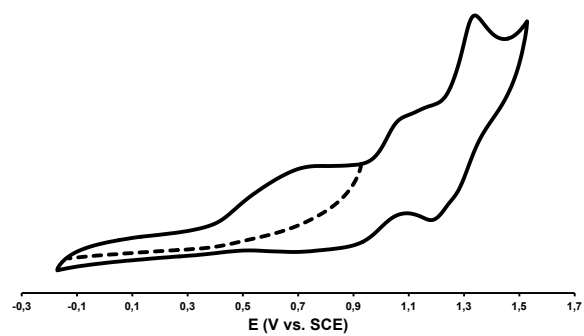
e) **12**
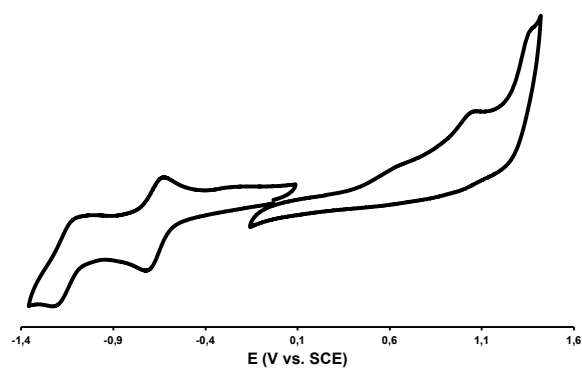
d) **14** (The first oxidation is due to ferrocene)
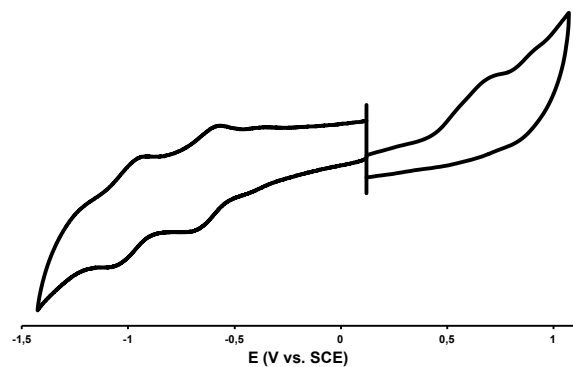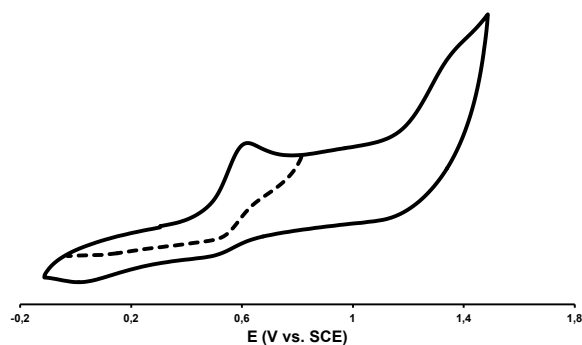
f) **15**

Fig. S37: Cyclic Voltammograms of **4a**, **12, 14** and **15** in CH_2Cl_2 containing 0.1 M of $[(nBu_4N)PF_6]$ at room temperature with a scan rate of 100 mV/s.

S7. References

1   M. J. Frisch, G. W. Trucks, H. B. Schlegel, G. E. Scuseria, M. A. Robb, J. R. Cheeseman, G. Scalmani, V. Barone, B. Mennucci, G. A. Peters- son, H. Nakatsuji, M. Caricato, X. Li, H. P. Hratchian, A. F. Izmaylov, J. Bloino, G. Zheng, J. L. Sonnenberg, M. Hada, M. Ehara, K. Toyota, R. Fukuda, J. Hasegawa, M. Ishida, T. Nakajima, Y. Honda, O. Kitao, H. Nakai, T. Vreven, J. A. Montgomery, Jr., J. E. Peralta, F. Ogliaro, M. Bearpark, J. J. Heyd, E. Brothers, K. N. Kudin, V. N. Staroverov, R. Kobayashi, J. Normand, K. Raghavachari, A. Rendell, J. C. Burant, S. S. Iyengar, J. Tomasi, M. Cossi, N. Rega, J. M. Millam, M. Klene, J. E. Knox, J. B. Cross, V. Bakken, C. Adamo, J. Jaramillo, R. Gomperts, R. E. Stratmann, O. Yazyev, A. J. Austin, R. Cammi, C. Pomelli, J. W. Ochterski, R. L. Martin, K. Morokuma, V. G. Zakrzewski, G. A. Voth, P. Salvador, J. J. Dannenberg, S. Dapprich, A. D. Daniels, O. Farkas, J. B. Foresman, J. V. Ortiz, J. Cioslowski and D. J. Fox, *Gaussian 09 Revision D.01*, 2009, Gaussian Inc. Wallingford CT.

2   Y. Zhao and D. G. Truhlar, *Acc. Chem. Res.*, 2008, **41**, 157.

3   Y. Zhao and D. G. Truhlar, *Theor. Chem. Acc.*, 2008, **120**, 215.

4   D. Jacquemin, E. A. Perpète, I. Ciofini, C. Adamo, R. Valero, Y. Zhao and D. G. Truhlar, *J. Chem. Theory Comput.*, 2010, **6**, 2071.

5   H. Audi, Z. Chen, A. Charaf-Eddin, A. D'Aléo, G. Canard, D. Jacquemin and O. Siri, *Chem. Commun.*, 2014, **50**, 15140.

6   J. Tomasi, B. Mennucci and R. Cammi, *Chem. Rev.*, 2005, **105**, 2999–3094.

7   R. Cammi, S. Corni, B. Mennucci and J. Tomasi, *J. Chem. Phys.*, 2005, **122**, 104513.

8   Turbomole v6.6 2014, a development of university of Karlsruhe and forschungszentrum karlsruhe gmbh, 1989-2007, turbomole gmbh, since 2007; available from http://www.turbomole.com (accessed 13 june 2016)

9   K. N. Raymond, *Chem. Eng. News,* 1983, **61**, 4.

10   P. Gans, and B. O'Sullivan, *Talanta,* 2000, **51**, 33.

11   (a) H. Gampp, M. Maeder, C. J. Meyer and A. D. Zuberbühler, *Talanta,* 1985, **32**, 95. (b) F. J. C. Rossotti, H. S.Rossotti, and R. J. Whewell, *J. Inorg. Nucl. Chem.,* 1971, **33**, 2051. (c) H. Gampp, M. Maeder, C .J. Meyer and A. D. Zuberbühler, *Talanta,* 1985, **32**, 257. (d) H. Gampp, M. Maeder, C. J. Meyer and A. D. Zuberbühler, *Talanta,* 1986, **33**, 943.

12   D. W. Marquardt, *J. Soc. Indust. Appl. Math.,* 1963, **11**, 431.

13   M. Maeder, and A. D. Zuberbühler, *Anal. Chem.,* 1990, **62**, 2220.

14   L. Alderighi, P. Gans, A. Ienco, D. Peters, A. Sabatini and A. Vacca, *Coord. Chem. Rev.*, 1999, **184**, 311.

15   J. F. Corbett; *J. Chem. Soc. (B)*, 1969, 213.

16   M. Novak and K. N. Martin; *J. Org. Chem.*, 1991, **56**, 213.

17   A. K. Ghosh, K. N. Mitra, G. Mostafa and S. Goswami; *Eur. J. Inorg. Chem.*, 2000, 1961.

18   S. P. Moulik, B. K. Paul, D. C. Mukherjee, *J. Col. & Interf. Sci.* 1993, **161**, 72.

19   M. Elhabiri, O. Siri, A. Sornosa-Tent, A.-M. Albrecht-Gary and P. Braunstein, *Chem. Eur. J.* 2004, **10**, 134.